Ocean Modelling 197 (2025) 102598

Contents lists available at ScienceDirect

Ocean Modelling

journal homepage: www.elsevier.com/locate/ocemod

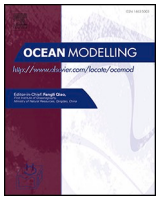

Evaluation of a 3D unstructured grid model for the New York-New Jersey Harbor under different forcing sources

Kyungmin Park [a,*], Y. Joseph Zhang [b], Emanuele Di Lorenzo [c], Gregory Seroka [d], Ayumi Fujisaki-Manome [e], Shachak Pe'eri [f], Saeed Moghimi [d], John G.W. Kelley [d]

[a] Coastal Sciences Division, Pacific Northwest National Laboratory, Seattle, WA, 98109, USA
[b] Virginia Institute of Marine Science, College of William & Mary, Gloucester Point, VA, 23062, USA
[c] Earth, Environmental, & Planetary Sciences, Brown University, Providence, RI, 02912, USA
[d] Coast Survey Development Laboratory, NOAA, Silver Spring, MD 20910, USA
[e] Cooperative Institute for Great Lakes Research (CIGLR), School for Environment and Sustainability, University of Michigan, Ann Arbor, MI, USA
[f] NOAA National Geodetic Survey, Silver Spring, MD, USA

ARTICLE INFO

Keywords:
Coastal ocean modeling
NY/NJ harbor
Sensitivity experiment
Forcing sources
Unstructured grid model
SCHISM

ABSTRACT

This paper presents an in-depth evaluation of a 3D unstructured grid model under various forcing sources, with a focus on the New York-New Jersey (NY-NJ) harbor. The model is first calibrated and evaluated through control runs, ensuring it accurately captures essential processes around the NY/NJ harbor. The sensitivity experiments highlight the significant roles and contributions of different forcing sources in coastal ocean conditions such as total water level, currents, salinity, and water temperature. Different tidal forcings, including FES2014, TPXO9 v1, and TPXO9 v5, show significant effects on tidal components, total water levels, currents, and water temperature, with minimal impact on salinity. Surface forcings from the HRRR, ERA5, and GFS demonstrate variable influences on water temperature predictions, while total water level, currents, and salinity are less sensitive to the different atmospheric forcing sources. Different open ocean conditions from CMEMS, HYCOM, and GRTOFS exhibited minor impacts on hydrodynamic variables in the inland rivers and estuaries but noticeably affected ocean surface currents and vertical structures of water temperature on the continental shelf. Different river discharges from USGS and NWM show high sensitivities of salinities and upstream water levels while shelf-scale ocean currents and vertical structures of water temperatures are similar across the different river discharges. The findings emphasize the necessity of selecting optimal forcing sources to minimize uncertainties and enhance predictive capabilities, supporting better decision-making in coastal management and hazard mitigation.

1. Introduction

Unstructured-grid models have played key roles in analyzing and forecasting the coastal ocean dynamics because the grid system provides high flexibility and efficiency for representing bathymetries, complex coastlines and inland rivers (Kernkamp et al., 2011). Therefore, the accuracy and reliability of coastal ocean models based on unstructured grids are critical for managing safe and efficient marine navigation and developing effective coastal protection and management plans, particularly in the context of climate change. The performance of the models depends on various factors, including the grid systems, numerical schemes, governing equations, compounding physical processes, and the uncertainties inherited in the forcing sources (Zhao et al., 2011; Chen et al., 2012; Li et al., 2015; Warder et al., 2021). Forcing sources, in the form of surface forcing and boundary conditions, derived from larger/global-scale models or observations, are crucial inputs for the coastal ocean models. With advancements in observational technologies and computational resources, modelers have had more opportunities to utilize diverse forcing sources. These advancements have improved the quality and resolution of data available for model inputs, enhancing the potential accuracy of the models by quantifying model uncertainties from the various forcings. However, each forcing source is still inherently characterized by some level of uncertainty, leading to uncertainties in model performance. This uncertainty introduces confidence limits that must be understood and accounted for when interpreting model results. However, comprehensive model evaluations

* Corresponding author.
E-mail address: kyungmin_park@brown.edu (K. Park).

https://doi.org/10.1016/j.ocemod.2025.102598
Received 21 August 2024; Received in revised form 9 January 2025; Accepted 15 July 2025
Available online 17 July 2025

and sensitivity experiments involving various forcing sources are relatively rare in coastal ocean areas. Such evaluations are essential to understand the strengths and limitations of different forcing sources and to improve the overall models' reliability. Therefore, examining cross-scale coastal ocean models using different forcing sources is imperative.

In this study, we evaluate various forcing sources for the tide, surface forcing, open ocean boundary conditions and river discharge based on available data from large/global scale models and observations. The tide is a key driver in coastal ocean dynamics, modulating mixing, coastal sea levels, and currents (Munk and Wunsch, 1998; Klymak et al., 2006; Huang et al., 2022). As a result, an accurate representation of tidal forcing in coastal ocean models is essential for predicting complex phenomena such as tidal flooding and the distribution of salinity, sediment, and nutrients. Surface forcing encompasses wind stress, air pressure, heat flux, precipitation and evaporation, as applied on the surface of coastal ocean models. Because surface forcing significantly affects coastal ocean dynamics, including upwelling/downwelling, mixed layer depth, coastal circulation, and storm surge, extensive sensitivity experiments have been conducted to investigate the uncertainties associated with surface forcing (Li et al., 2015, 2016; Warder et al., 2021; Astudillo et al., 2019; Dinápoli et al., 2020). Given the considerable influence of surface forcing on coastal ocean dynamics, it is important to achieve a better understanding of how sensitive coastal ocean models are to variations in atmospheric conditions to improve model accuracy. Open ocean boundary conditions represent the impacts of larger-scale oceanic processes, such as changes in sea levels, currents, water temperature, and salinity gradients on the open boundary. To reduce computational costs, high-resolution coastal ocean models are often downscaled within limited areas (Trotta et al., 2021). During downscaling, the open boundary of the coastal ocean model is constrained or nested by larger-scale models or observations, providing data on sea surface height, water temperature, salinity, and currents. The open ocean boundary condition can play a significant role in coastal sea levels as remote forcing (Park et al., 2022) and also influences three-dimensional hydrodynamic variables in advanced baroclinic coastal ocean models (Park et al., 2024; Ye et al., 2020). Proper implementation of open boundary conditions allows coastal ocean models to more accurately simulate the exchange of properties between the coastal and open ocean, thereby enhancing overall model fidelity. Coastal regions are often characterized by complex networks of multi-scale channels and rivers that deliver freshwater into estuaries and adjacent coastal waters. River discharge plays a pivotal role in shaping estuarine mixing and circulation, thereby influencing the spatial distribution of salinity and sediments (Warner et al., 2020; Lane et al., 2007). Furthermore, river flows significantly impact water levels and contribute to riverine and compound flooding during extreme weather events (Merz et al., 2021; Bermúdez et al., 2021). Therefore, the accurate representation of river discharge in coastal ocean models is essential for improving predictions of natural disasters and facilitating effective resource management.

Because there are various sources of the different forcings with inherent uncertainties, this study aims to characterize, contrast and understand these uncertainties, which serves as a companion to Zhang et al. (2024), where we have expounded on the importance of bathymetry as one of the most fundamental forcings in coastal regimes, and explained the detrimental consequences of models that do not respect it. However, we do not include the discussion on model sensitivity to different parameterizations due to two reasons. First, parameterizations have been extensively covered in previous literature (Ezer and Mellor, 2000; Li et al., 2015; Bastidas et al., 2016; Schroeter and Sandery, 2022). Second and perhaps more importantly, more precise and extensive observations are needed to quantify the uncertainty of those parameterizations (e.g., bottom friction), and therefore presently, most models treat those as tunable handles.

To achieve the goal, we perform a series of sensitivity experiments using a three-dimensional unstructured coastal ocean model. The experiment allows us to investigate the distinct roles and contributions of each forcing source in a coastal ocean system. Additionally, the experiments with different forcing scenarios, such as tide, surface forcing, open ocean boundary condition and river discharge, help identify which hydrodynamic variables are most sensitive to the different forcings. Understanding these sensitivities is important for enhancing the accuracy and reliability of coastal ocean models. The findings from this study will provide guidelines for better accuracy and confidence in coastal ocean modeling systems, ultimately contributing to more effective and sustainable coastal management practices. The details of the unstructured-grid model used in this study are presented in Section 2. We show and elucidate the results of model evaluations and sensitivity experiments in Section 3. The final conclusions and discussions are described in Section 4.

2. Methodology

2.1. Unstructured grid model SCHISM

The Semi-implicit Cross-scale Hydroscience Integrated System Model (SCHISM) represents a new generation of three-dimensional baroclinic models utilizing an unstructured grid system. The mesh system of the model uses mixed triangular-quadrangular elements. Furthermore, the model allows the use of Localized Sigma Coordinates with Shaved Cells (LSC^2) to enable variable vertical grids based on the underlying bathymetry (Zhang et al., 2015). The SCHISM's versatile 3D grid system enables efficient cross-scale modeling from the open ocean to the intricate networks of inland waterways, as elaborated by Zhang et al. (2016), Yu et al. (2017) and Ye et al. (2020). Employing a semi-implicit Galerkin finite-element methodology, SCHISM demonstrates precision and robustness in solving the Navier-Stokes equations within the constraints of hydrostatic and Boussinesq approximations. Within its sophisticated numerical framework, the model employs a semi-implicit scheme for the treatment of the divergence term, barotropic pressure gradient and vertical viscosity to bypass the stringent CFL stability constraint. The implicitness of 0.6 is considered in this study. Conversely, the model treats the baroclinic pressure gradient and horizontal viscosity with an explicit scheme. In this study, the transport equations for water temperature and salinity are solved using a Total Variation Diminishing second-order (TVD^2) implicit transport solver, offering precision and computational efficiency across a wide range of Courant numbers. For the three-dimensional continuity and scalar transport equations, SCHISM relies on finite-volume solvers, thereby ensuring the conservation of both volume and scalar quantities. Turbulent processes are modeled via the Generic Length Scale (GLS) model (Umlauf and Burchard, 2003)

2.2. Target area and computational mesh

The model domain covers the New York/New Jersey (NY/NJ) Bight, as shown in Fig. 1(a). Because the area has a complex network of narrow navigation channels, accurate predictions are crucial for both safe navigation and hydrodynamics. Given its importance, different operational forecast systems have been implemented in the regions, such as NYOFS (Wei and Chen, 2001) and NYHOPS (Georgas et al., 2016). In addition, the NY/NJ bight not only provides a suitable example of coastal ocean systems affected by various forcing (e.g., tide, river discharge, wind, precipitation and baroclinicity) but also includes the area of the NY/NJ harbor that is part of the coordinated marine navigation model evaluation effort of NOAA's Unified Forecast System (UFS) Coastal Applications Team (Seroka et al., 2022, 2024). The computational grid used in this study is constructed based on the available Digital Elevation Models (DEMs), encompassing only water bodies without land since inland inundation is outside the scope of this study. Various resolutions of DEMs (from 5 m to 2 km) are combined and interpolated for the mesh generation and model's bathymetry. The inherent stability and robustness of SCHISM allow the adoption of original, unsmoothed

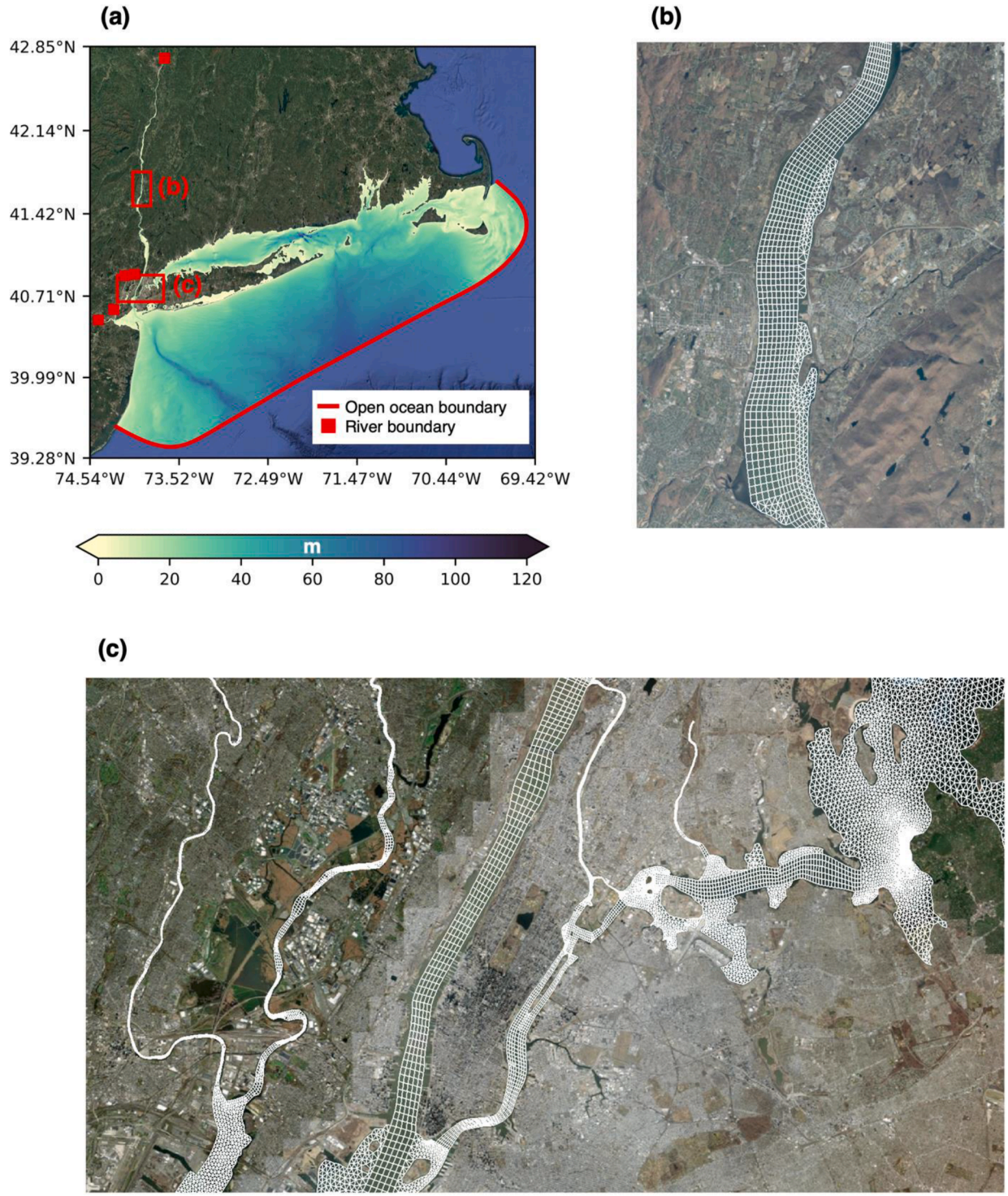

Fig. 1. (a) The model domain with interpolated bathymetry. The red line represents the open ocean boundary of the model, while the red boxes denote the inland river boundaries. The outlined red boxes indicate the zoom-in views of the computational mesh for (b) the Hudson River and (c) Manhattan.

bathymetries from the DEMs, thus enhancing the fidelity and accuracy of the simulations. This practice also improves the representation of key processes and minimizes errors from using manipulated, unrealistic bathymetries, making the results more defensible (Zhang et al., 2024). High-resolution grids (up to 5 m) are applied in the NY/NJ harbor and surrounding rivers to capture geographical features and station locations properly, while relatively coarse resolution grids (3.8 km) are used for the open boundaries. The computational mesh consists of both triangular and quadrangular elements. Fig. 1(b) and (c) provide a detailed representation of the mesh as close-up views. Quadrangular elements are used to delineate the main rivers such as Hudson, Hackensack, Passaic, Rahway, and Raritan Rivers efficiently, as shown in Fig. 1(b). Triangular elements are utilized to trace the complex coastlines accurately, as presented in Fig. 1(c). The resulting mesh comprises 95,566 nodes and 165,132 elements, with horizontal resolution varying from 3.8 km at the open boundary to 5 m within inland rivers. Additionally, the LSC^2 vertical grid system is employed for three-dimensional simulations, offering the flexibility of variable vertical layering to

accommodate bathymetric variations while enhancing stability. Accordingly, the number of vertical layers ranges from 1 in shallow waters to 33 in deeper oceans, yielding highly efficient three-dimensional simulations.

2.3. Model setup

In this study, we utilize SCHISM version 5.10 to evaluate model performances under different forcing sources. The model provides 3-D baroclinic simulation with a time step of 120 s. The uniform bottom roughness length of 0.005 m is prescribed across the modeling domain. Wind stress calculations were performed based on the algorithm proposed by Hwang (2018). In order to refine the model's accuracy in simulating scalar fields such as water temperature and salinity, the background diffusivity in the Hudson River is adjusted to a lower magnitude (i.e., 1e-6) in comparison to other regions (1e-4). The calibration results in improvements in the representation of salinity and water temperature distribution, underscoring the benefits of regional calibration over a uniform diffusivity approach across the entire domain.

We conduct numerical experiments to assess and quantify the sensitivity of model results to various forcing sources for tides, river discharge, surface forcing, and open ocean boundary conditions. Tidal forcing is obtained from three different sources: Finite Element Solution (FES) 2014 (Lyard et al., 2021), TOPEX/POSEIDON global tidal model (TPXO) 9 v1 and TPXO9 v5 (Egbert and Erofeeva, 2002). These models provide information on tidal components for an open ocean boundary condition, as shown in Fig. 1(a), and a body force in the momentum equation, incorporating eight significant tidal constituents: K1, K2, M2, N2, O1, P1, Q1, and S2. Open ocean boundary conditions such as sea surface height, three-dimensional water temperature, salinity, and currents are derived from the Copernicus Marine Environment Monitoring Service (CMEMS; Lellouche et al. 2018), the Hybrid Coordinate Ocean Model (HYCOM; Chassignet et al., 2007), and the Global Real-Time Ocean Forecast System (G-RTOFS; Garraffo et al., 2020). The variables from these large/global-scale oceanic models are imposed on the open ocean boundary, as presented in Fig. 1(a). Surface forcings, including wind velocities, atmospheric pressure, air temperature, and precipitation, utilize outputs from various atmospheric models such as the NOAA Global Forecast System (GFS), the European Centre for Medium-Range Weather Forecasts (ECMWF) Reanalysis v5 (ERA5; Hersbach et al., 2020), and the NOAA High-Resolution Rapid Refresh (HRRR, Dowell et al. 2022) model. River discharge data for the Hackensack, Passaic, Rahway, Raritan and Hudson Rivers are sourced from United States Geological Survey (USGS) observations and National Water Model (NWM; Cosgrove et al., 2024). The locations of the river inflows are indicated in Fig. 1(a). Table 1 shows the summary of the experiments using the different forcing sources. Note that, other than the targeted forcing source, the model configurations and grid are maintained consistently across all experiments to isolate the effect of the forcing source on model results.

2.4. Target period

This study evaluates the numerical model across two distinct periods: 2021 period (2021-July-1 to 2021-Oct-1) and 2022 period (2022-Jan-01 to 2022-April-01). The first period includes the Summer and Fall seasons (SF), while the second period has the Winter and Spring (WS). These periods are selected due to their capacity to delineate the seasonality in various forcing factors such as wind stress, air pressure, air temperature, heat flux, ocean temperature, currents, and salinity in the NY/NJ region. Accordingly, the sensitivities of the model results regarding the different forces can also be assessed in the context of seasonal variations. In addition, we evaluate the model performance under extreme weather conditions because the selected time periods include Hurricane Elsa (2021-June-30 to 2021-July-9), Hurricane Henri (2021-August-15 to 2021-August-25), Hurricane Ida (2021-August-25 to 2021-September-4), Hurricane Ida (2021-August-25 to 2021-September-4) and Nor'easters (2022-January-14 to 2022-January-21). Following a one-month spin-up period for each time frame, the subsequent three-month simulation results are systematically compared against observations for model evaluations.

Table 1
Summary of the sensitivity experiments.

Period	Experiment	Open boundary forcing	Surface forcing	Tidal forcing	River forcing
2021-July-01 to 2021-Oct-01 Summer to Fall	SF-CR	CMEMS	HRRR	FES2014	USGS
	SF-TP1	CMEMS	HRRR	TPXO9 v1	USGS
	SF-TP5	CMEMS	HRRR	TPXO9 v5	USGS
	SF-ER	CMEMS	ERA5	FES2014	USGS
	SF-GF	CMEMS	GFS	FES2014	USGS
	SF-HY	HYCOM	HRRR	FES2014	USGS
	SF-GR	GRTOFS	HRRR	FES2014	USGS
	SF-RF	CMEMS	HRRR	FES2014	NWM
2022-Jan-01 to 2022-April-01 Winter to Spring	WS-CR	CMEMS	HRRR	FES2014	USGS
	WS-TP1	CMEMS	HRRR	TPXO9 v1	USGS
	WS-TP5	CMEMS	HRRR	TPXO9 v5	USGS
	WS-ER	CMEMS	ERA5	FES2014	USGS
	WS-GF	CMEMS	GFS	FES2014	USGS
	WS-HY	HYCOM	HRRR	FES2014	USGS
	WS-GR	GRTOFS	HRRR	FES2014	USGS
	WS-RF	CMEMS	HRRR	FES2014	NWM

2.5. Observations and model evaluations

We perform model assessments, leveraging various observations from USGS, NOAA/National Ocean Service stations of the National Water Level Observing Network, New York/New Jersey Harbor Physical Oceanographic Real-Time System (PORTS), National Estuarine Research Reserve System's System-wide Monitoring Program (SWMP) and NJDEP Marine Water Monitoring Program. These observations encompass tidal constituents, total water levels, currents, water temperatures and salinities, which are comprehensively compared with model results. Fig. 2 shows the spatial distribution of the observational points for each variable. Tidal constituents and total water levels are collected not only around the NY/NJ harbor, but also the Long Island Sound and Great South Bay, as illustrated in Fig. 2(a) and (b). For current velocity profiles across different depths, a PORTS Acoustic Doppler Current Profiler (ADCP) is used within the Kill Van Kull (KVK), a key navigation channel, as indicated in Fig. 2(b). The depths of the ADCP range from 3.5 to 15.5 m with about 1 m intervals. Water temperature and salinity observations span from the Lower Bay to the upper stretches of the Hudson River, as displayed with red circles in Fig. 2(c) and (d).

Table 2 shows the detailed locations of the stations for the tidal constituents, while Table 3 lists the stations for total water levels and currents. Table 4 shows the details of the water temperature and salinity observations. The availabilities of the water temperature and salinity observations depend on the year, and they are listed in Table 4. In addition to the point-based observations, we utilize High Frequency (HF) Radar data from the Integrated Ocean Observing System and Expendable Bathythermograph (XBT) from the Ship Oleander Project (https://www.aoml.noaa.gov/phod/goos/oleander/intro.php) to evaluate the model performance in simulating shelf-scale ocean currents and vertical distribution and stratification of ocean temperatures. The spatial data from these observations provide opportunities to evaluate how well the model reproduces the oceanic processes in the open ocean and continental shelf areas. The extensive observational data enables a comprehensive assessment of the model across various geographical features and marine environments, ensuring a robust validation and evaluation of the model's capabilities.

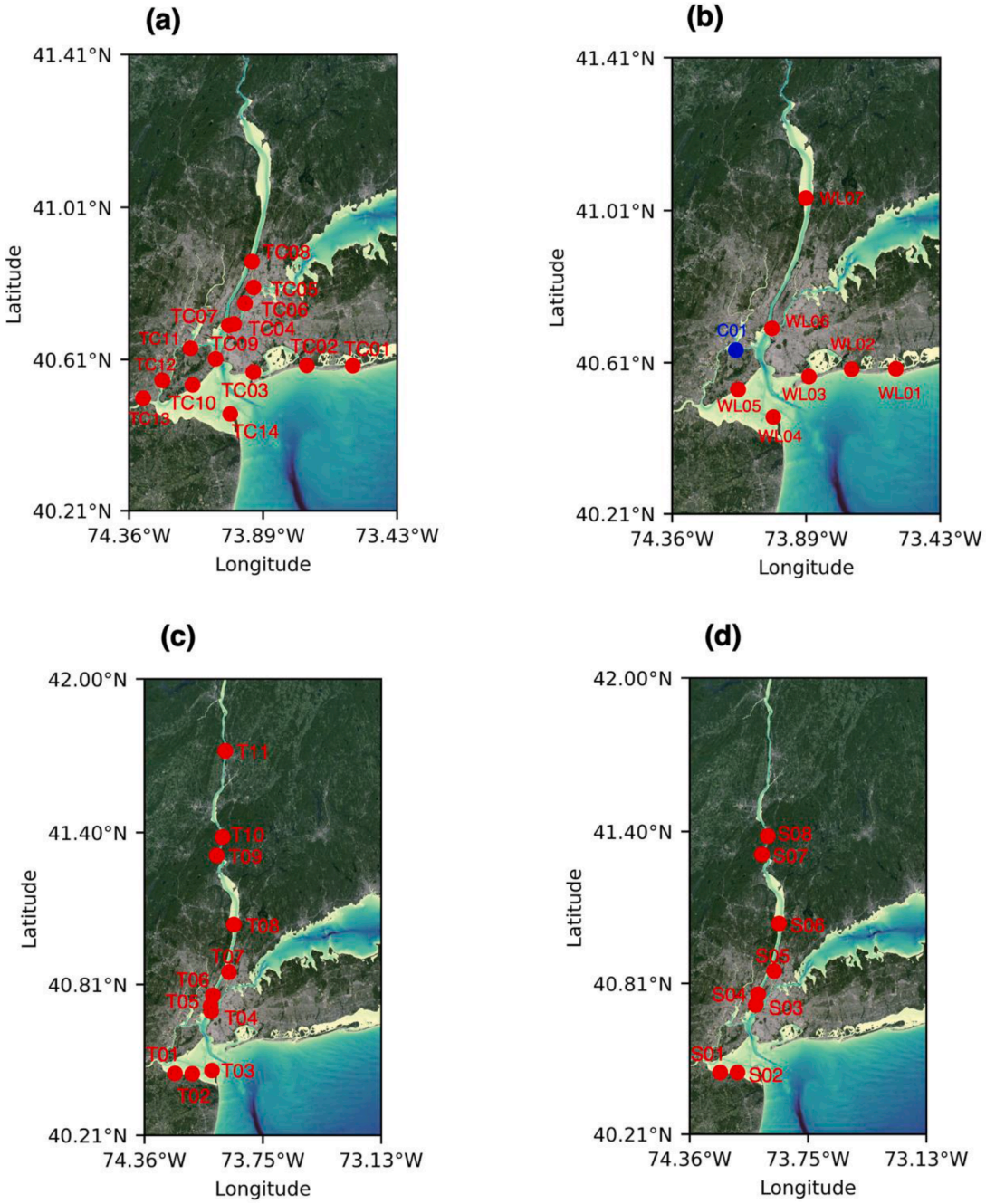

Fig. 2. The locations of observation for the (a) tidal constituents (red) (b) total water levels (red) and currents (blue), (c) water temperatures (red) and (d) salinities (red).

In this study, we utilize different statistics that compare the model results against the observations as follows:

Bias:

$$\frac{1}{N}\sum_{1}^{N}(M_i - O_i) \quad \text{(Eq. 1)}$$

Root-mean-square-error (RMSE):

$$\sqrt{\frac{1}{N}\sum_{1}^{N}(M_i - O_i)^2} \quad \text{(Eq. 2)}$$

Complex error:

$$\sqrt{\left((A_o cosP_o - A_m cosP_m)^2 + (A_o sinP_o - A_m sinP_m)^2\right)/2} \quad \text{(Eq. 3)}$$

Where M_i, O_i, and N, are the modeled, observed values and number of samples. The bias quantifies the average discrepancy between modeled and observed values, serving as an indicator of systematic overestimation or underestimation by the model. The RMSE measures the magnitude of discrepancies between modeled and observed values, offering insights into the model's overall precision. The complex error considers both amplitude and phase to quantify errors between observed and modeled values in a complex plane (Foreman et al., 1993). By using the three statistics, we conduct the model assessment in the following section.

Table 2
The stations for tidal constituents.

Tidal constituents			
	Longitude	Latitude	Station ID
TC01	−73.584100	40.594085	NOAA 8516402
TC02	−73.743231	40.594446	NOAA 8516881
TC03	−73.9291	40.5773	NOAA 8517756
TC04	−73.995604	40.703905	NOAA 8517847
TC05	−73.9283	40.8	NOAA 8518643
TC06	−73.9583	40.7583	NOAA 8518687
TC07	−74.013766	40.700554	NOAA 8518750
TC08	−73.933772	40.868383	NOAA 8518902
TC09	−74.0599	40.612	NOAA 8519050
TC10	−74.14	40.5433	NOAA 8519436
TC11	−74.147487	40.639862	NOAA 8519483
TC12	−74.245	40.555	NOAA 8531142
TC13	−74.3117	40.5083	NOAA 8531262
TC14	−74.0094	40.4668	NOAA 8531680

Table 3
The stations for total water level and currents. SF and WS mean Summer-Fall and Winter-Spring seasons.

Water level				
	Longitude	Latitude	Station ID	Availability
WL01	−73.583739	40.593436	USGS 01310740	SF and WS
WL02	−73.737354	40.593160	USGS 01311145	SF and WS
WL03	−73.885136	40.573716	USGS 01311875	SF and WS
WL04	−74.009400	40.466800	NOAA 8531680	SF and WS
WL05	−74.129888	40.538888	USGS 01376562	SF and WS
WL06	−74.014200	40.700600	NOAA 8518750	SF and WS
WL07	−73.896055	41.043194	USGS 01376269	SF and WS
Currents				
	Longitude	Latitude	Station ID	Availability
C01	−74.138890	40.643580	NOAA n06010	SF and WS

Table 4
The stations for water temperature and salinity. SF and WS mean Summer-Fall and Winter-Spring seasons.

Temperature				
	Longitude	Latitude	Station ID	Availability
T01	−74.201066	40.455616	RB02 NJBuoy_8	SF
T02	−74.112017	40.454883	RB01 NJBuoy_7	SF
T03	−74.0094	40.4668	8531680	WS
T04	−74.013766	40.700554	8518750	SF and WS
T05	−74.016704	40.721731	01376520	WS
T06	−74.004678	40.764769	01376515	SF and WS
T07	−73.921079	40.855477	01302025	SF
T08	−73.896	41.043	01376269	SF and WS
T09	−73.984163	41.314018	BM HBMN6	SF and WS
T10	−73.954023	41.386127	1374019	SF and WS
T11	−73.940692	41.72176	1372043	SF and WS
Salinity				
	Longitude	Latitude	Station ID	Availability
S01	−74.201066	40.455616	RB02 NJBuoy_8	SF
S02	−74.112017	40.454883	RB01 NJBuoy_7	SF
S03	−74.016704	40.721731	01376520	WS
S04	−74.004678	40.764769	01376515	WS
S05	−73.921079	40.855477	01302025	SF
S06	−73.896	41.043	01376269	SF and WS
S07	−73.984163	41.314018	BM HBMN6	SF and WS
S08	−73.954023	41.386127	1374019	SF and WS

3. Result

3.1. Control run evaluation

We calibrate and evaluate the control runs (e.g., SF-CR and WS-CR) first, which serves as a reference point for the sensitivity experiments in the next section (e.g., 3.2 Sensitivity experiments). The control runs represent the controlled conditions against experiments with different forcing sources. By comparing the control runs with other experiments, we can investigate the relative contributions of different forcing sources on the model performance. The evaluation of the control runs also ensures that the model used in this study properly captures essential processes in the NY/NJ harbor so that the finding from this study establishes credibility.

3.1.1. Tidal constituents

The fidelity of the numerical model in predicting tidal constituents is evaluated by comparing the modeled constituents against in situ observations. A suite of 14 NOAA stations provides comprehensive data on tidal constituents. The details of the stations are presented in Fig. 2 and Table 2. Harmonic analyses are performed on the model output to extract the amplitudes and phases for primary tidal constituents, focusing on M2 due to its predominance along the U.S. East Coast (Huang et al., 2022). Fig. 3 presents modeled and observed M2 amplitudes and phases at the different stations. The model properly reproduces the M2 constituent, yielding RMSEs for amplitudes of 1.83 cm in the Summer-Fall season (SF-CR) and 2.25 cm in the Winter-Spring season (WS-CR). The RMSEs for phases are 4.64° for SF and 5.00° for WS, implying a good temporal alignment of the tidal cycles with observed data. Adopting the methodology of Foreman et al. (1993), we employ a complex error metric (Eq. (3)) that considers both amplitude and phase deviations on a complex plane. This comprehensive measure reveals RMS complex errors of 2.58 cm for SF and 3.05 cm for WS across all evaluated stations. The model's statistical metrics convincingly explain its capability to approximate tidal dynamics with high reliability in the NY/NJ harbor region for both SF and WS seasons.

3.1.2. Total water level

Fig. 4 presents the biases (Eq. (1)) and RMSEs (Eq. (2)) for total water levels in 2021 and 2022. Specifically, Fig. 4(a) and (b) show the statistics for the SF season, while Fig. 4(c) and (d) provide corresponding values for the WS season. It is apparent that the model predicts water levels with higher accuracy in SF than in WS. For example, the biases and RMSEs highlight the seasonal difference in model performance. In the WS season, the model tends to underestimate water levels more than in SF, as shown in Fig. 4(a) and (c). The difference is associated with the prevalence of higher water levels during WS due to seasonal variability, such as increased wind stress and air pressure gradients, as well as the influence of more dynamic remote oceanic forces through open boundary conditions. These factors are further compounded by episodic extreme events, such as winter storms and Nor'easters, which are more challenging for the model to capture effectively, leading to greater negative biases. This is particularly evident in the nontidal residual (NTR) of total water levels shown in Supplementary Figure 1. Similarly, RMSE values are higher in WS than in SF, as shown in Fig. 4(b) and (d), reflecting the combined influence of seasonal variability and extreme events. The principal contributors to this discrepancy are the uncertainties associated with atmospheric conditions, such as wind stress and air pressure, and remote oceanic forces that influence the NTR through its open boundary conditions. These factors play important roles in abnormal water levels during extreme weather conditions, as discussed in the study by Park et al. (2022). We further evaluate the model's accuracy in simulating extreme coastal hazards by analyzing the peak water levels and their timing during selected extreme events including Hurricanes Elsa, Henri, Ida, Sam, and Nor'easters. As presented in Supplementary Tables 1 and 2, the model effectively captures

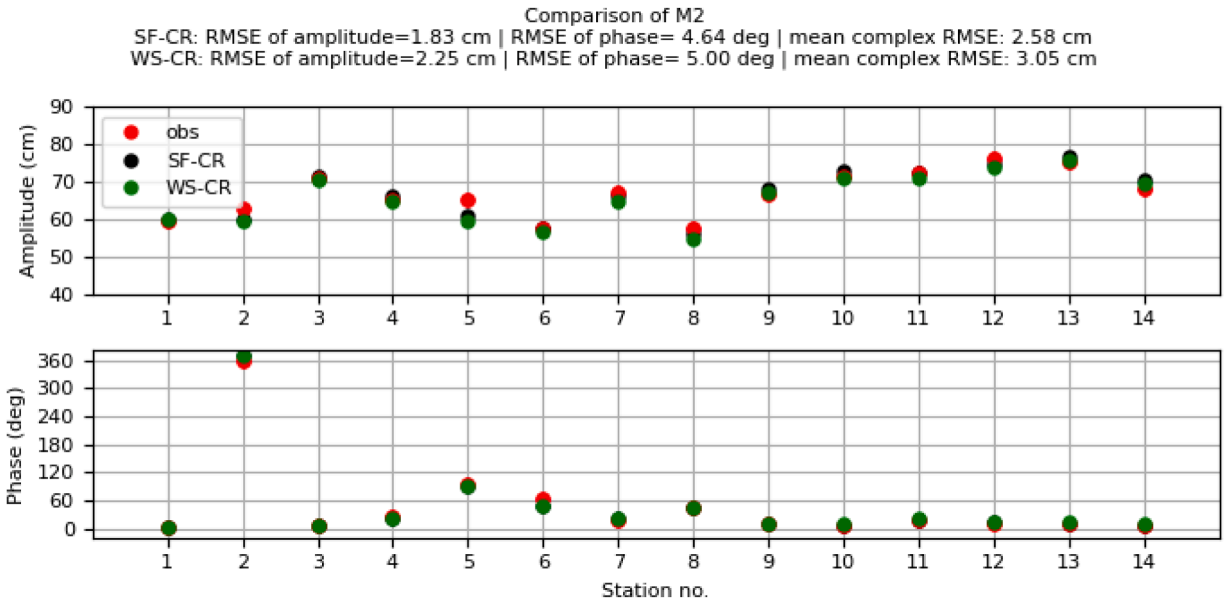

Fig. 3. The comparison of the M2 amplitudes and phases between observation and control runs (i.e., SF-CR for the summer-fall season and WS-CR for the winter-spring season).

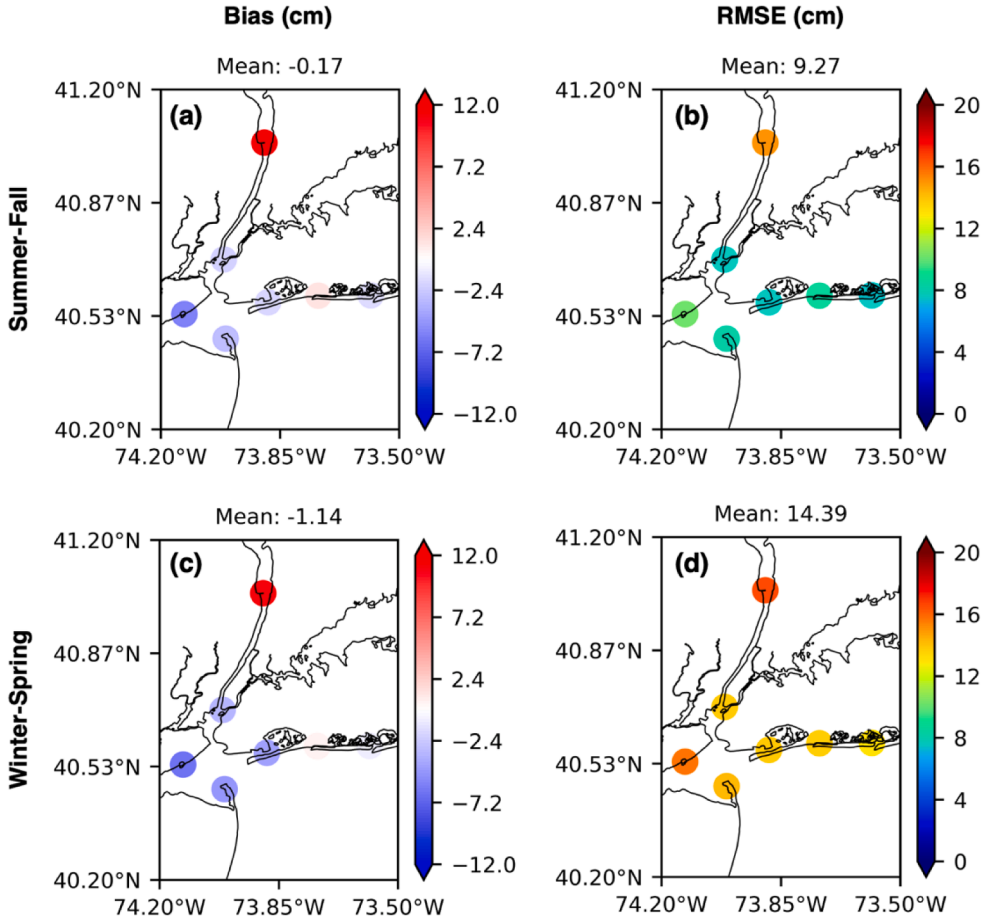

Fig. 4. The biases (m) and RMSEs (m) for the total water levels from control runs (i.e., SF-CR and WS-CR). The top and bottom rows represent the statistical indexes for the summer-fall and winter-spring seasons, respectively.

the observed peaks and timing of abnormal water levels during these events. These findings highlight the model's reliability in representing critical storm surge characteristics, offering valuable insights for hazard prediction and coastal management applications.

The biases of water levels around the coast are generally small (about ± 2 cm) for both seasons while an exception is found upstream of the

Hudson River (e.g., WL07 in Fig. 2). Here, a high positive bias of up to 12 cm is observed, indicating the lowest modeling skill in this particular location, as presented in Fig. 4(a) and (c). This discrepancy is largely attributed to uncertainties in river discharge data and the accuracy of digital elevation models (DEMs) over the river. The inaccuracy of river discharge data is particularly problematic because of the limited measurements available in the NY/NJ harbor, as the USGS station in Albany (USGS 01358000) becomes the Hudson River's closest upstream data collection point. Combining the limited information with uncertainties inherent in DEMs results in unrealistic river flow downstream, causing increased errors in water level predictions in the region, such as at WL07. Furthermore, areas exhibiting high biases often correlate with narrow piers that are poorly represented in the DEM data, as illustrated in Supplementary Figure 2. As a result, the highest RMSEs for the SF (15 cm) and WS (16 cm) are observed at the WL07. Meanwhile, RMSEs for other coastal areas are more modest, ranging from 8 to 10 cm for the SF season and from 13 to 14 cm for the WS season, suggesting a more reliable model performance in these regions.

3.1.3. Currents

For the current assessment, we compared modeled ocean currents with the measurements from HF Radar and ADCP near the NY/NJ harbor. Fig. 5 shows the spatial distributions of biases and RMSEs for the summer-fall (SF-CR) and winter-spring (WS-CR) seasons. Considering uncertainty inherited in the HF Radar (Xu et al., 2022; Fang et al., 2015), we exclude the observations with Dilution of Precision (DOP) of below 0.3 and shallow water depths of below 40 m for the comparison between the model and observation. To calculate the statistical parameters, we interpolate the modeled surface currents onto the HF radar's grid with the observation's temporal resolution. Note that although the HF Radar's coverage does not extend into the inland channels of the NY/NJ harbor, the observation provides valuable insights into the model's predictive capabilities across the continental shelf area. Our statistical evaluation reveals the model exhibits high predictive skill across most surveyed regions, achieving a mean RMSE of 15.34 cm/s (SF) ~ 12.81 cm/s (WS). The RMSEs for both seasons increase as they go to the shelf break and northeast, where the open boundary condition of the model exists. Therefore, the high RMSEs can be affected by the uncertainties from the open boundary condition. For this reason, the RMSEs are highest in these areas, showing RMSE of up to 20 cm/s, while the RMSEs decrease to 6 ~ 10 cm/s when it is close to the NY/NJ harbor and the coast. The bias maps indicate general overestimations of ocean currents by the model, showing mean biases of 7.23 cm/s for SF and 6.44 cm/s for WS.

In addition to the HF radar, we assess the modeled currents over depth with an ADCP measurement. This ADCP is located in the inland channel of the NY/NJ harbor, specifically in the KVK, as illustrated in Fig. 2. Our analysis utilizes the Principal Component Direction (PCD) of currents, a quantitative measure of the predominant flow direction within the channel. By analyzing the PCD, we evaluate the model's accuracy for the dominant directional flow across the different depths extending from 3.5 to 15.5 m at approximately 1-m intervals, as recorded by the ADCP. Table 5 shows not only errors in the PCD between our model and the observation but also RMSEs and biases for the current speed along the PCD at varying depths. The model results closely match the PCD derived from the ADCP, showing that the depth-averaged errors of the PCDs are −2.54 and 2.67 degrees for the SF and WS seasons, respectively. The depth-averaged RMSEs for the current speed along the PCD are 12.46 and 13.61 cm/s for the SF and WS seasons, respectively. The higher RMSE during WS than SF is primarily attributed to higher uncertainties of forcing sources associated with the seasonality, extreme weather and resulting river discharges on the inland rivers. In general,

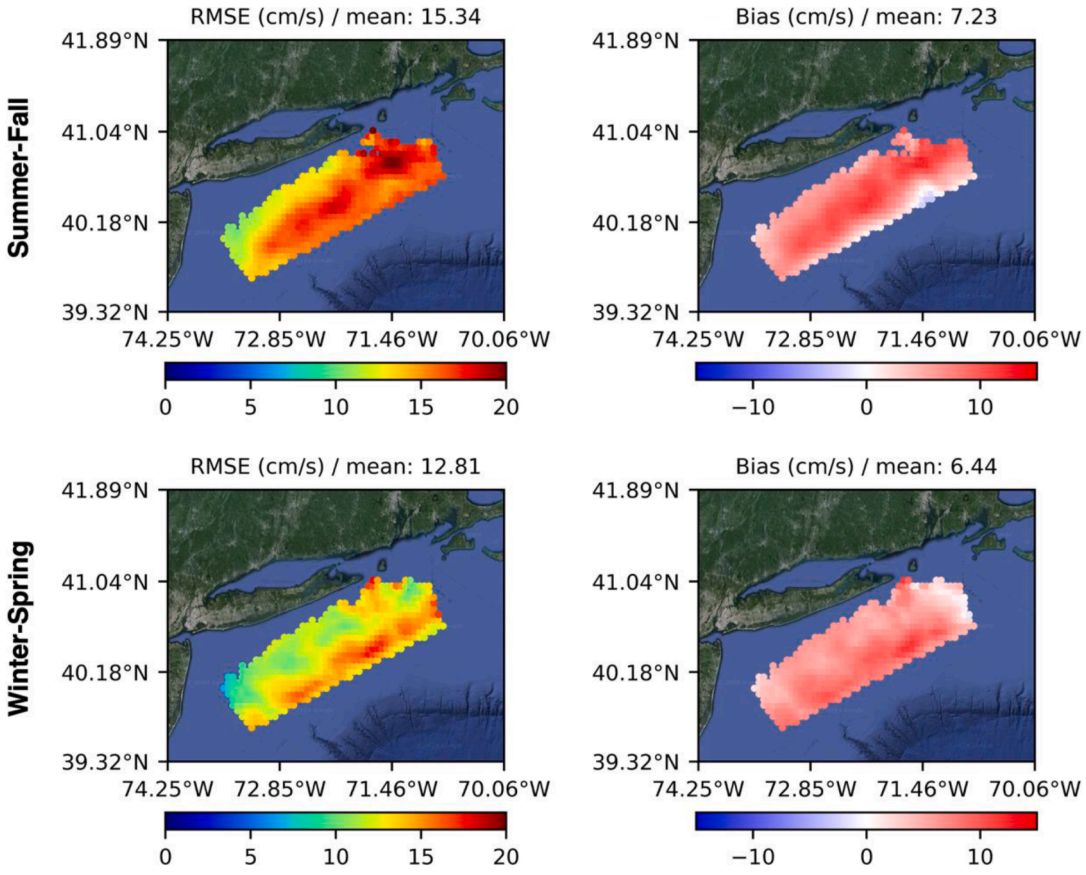

Fig. 5. Spatial map of RMSEs and Biases for the ocean surface currents from control runs (i.e., SF-CR and WS-CR). The top and bottom rows represent the spatial maps for the summer-fall and winter-spring seasons, respectively.

Table 5
Current assessment along the Principal Component Direction (PCD) at C01.

Experiments	Index	Depth	Speed RMSE (cm/s)	Speed bias (cm/s)	Direction error (deg)
2021	C01	3.5 m	12	2	−3.99
	C01	4.5 m	11	3	−5.07
	C01	5.5 m	12	4	−4.82
	C01	6.6 m	12	4	−4.42
	C01	7.5 m	13	4	−4.03
	C01	8.5 m	13	4	−3.54
	C01	9.5 m	13	4	−3.01
	C01	10.5 m	13	5	−2.54
	C01	11.6 m	13	5	−2.18
	C01	12.5 m	13	6	−2.03
	C01	13.5 m	13	7	−1.83
	C01	14.5 m	12	7	−1.36
	C01	15.5 m	12	6	−0.17
	Mean		**12.46**	**4.69**	**−2.54**
2022	C01	3.5 m	14	−1	2.24
	C01	4.5 m	13	0	2.88
	C01	5.5 m	13	0	3.03
	C01	6.6 m	13	1	1.93
	C01	7.5 m	13	1	1.65
	C01	8.5 m	13	1	2.31
	C01	9.5 m	14	2	2.73
	C01	10.5 m	14	3	3.26
	C01	11.6 m	14	4	3.11
	C01	12.5 m	14	5	3.05
	C01	13.5 m	14	5	2.66
	C01	14.5 m	14	6	2.61
	C01	15.5 m	14	6	3.34
	Mean		**13.61**	**2.53**	**2.67**

the model shows the overestimations of the currents with depth-averaged biases of 4.69 cm/s for SF and 2.53 cm/s for WS.

3.1.4. Water temperatures

We investigate the biases and RMSEs for water temperature with seasonal differences, as presented in Fig. 6. Specifically, Fig. 6(a) and (b) show the SF season, while Fig. 6(c) and (d) correspond to the WS season. Our findings reveal a notable distinction in model performance between the two seasons because the SF season shows lower RMSEs and biases than the WS as shown in Fig. 6. Fig. 6(a) and (c) show that the biases in temperature are negative for both seasons, averaging −0.53 °C in the summer and −1.81 °C in the WS. These persistent cold biases suggest a systemic underestimation of water temperatures, which is partially attributed to surface forcing and initial and boundary conditions from the large-scale oceanic and atmospheric models used in this study. For example, a forcing source (e.g., HRRR) exhibits cold biases in air temperatures (Supplementary Fig. 3), which implies the impact of forcing source uncertainties on our model results. The extent of the biases varies seasonally, showing more pronounced cold biases in WS than in the summer. In addition, air temperatures during the WS season often plunge below freezing, as presented in Supplementary Figure 3, which can lead to sea ice formation. In fact, there was some river ice reported upstream of the Hudson River (NWS, 2022a,b). However, our model does not incorporate an ice model that can reproduce the insulating effect of sea ice, which can contribute to the colder biases in the WS season. In addition, the model does not include the large thermal discharges from emergency power plants in the area, as applied in another model (e.g., NYHOPS; Georgas et al., 2016), which can cause additional colder biases of the water temperature on the rivers. The RMSEs in Fig. 6 (b) and (d), following the spatial patterns of the biases, display high RMSEs downstream compared to upstream of the Hudson River. In addition, the higher RMSEs for temperature during WS than SF are a direct consequence of the increased cold biases, highlighting the season-specific challenge associated with the winter weather conditions. These findings not only underscore the significance of accounting for seasonal variability of the air temperature but also emphasize the need for refining the representation of forcing sources and incorporating ice processes to enhance winter season modeling.

Fig. 7 shows the vertical temperature profiles derived from both the numerical model and the XBT from the Ship Oleander Project. The profiles depict the thermal gradients across varying depths at distinct observation points, as presented in Fig. 7. During the SF season, as highlighted in the left column of Fig. 7, both the model and observations consistently exhibit stratified temperature fields through the water column. This stratification is predominantly driven by the augmented intensity and persistence of solar radiation, which results in a pronounced thermal separation between the warmer surface waters and the colder deep water. Nonetheless, it reveals certain inaccuracies, specifically a tendency to underestimate the surface temperatures within the upper 20 m, indicating a negative bias, while simultaneously overestimating temperatures between the 20 to 70-meter depths, showing a positive bias. The differences reflect less pronounced temperature stratification by the model compared to actual observations. Conversely, the WS season, illustrated in the right column of Fig. 7, shows that the observed temperature profiles exhibit well-mixed vertical distribution due to the diminished solar radiation and amplified wind mixing effects. The temperature gradient is observed along the observation points from the estuary (colder) to the open ocean (warmer). The model properly simulates the well-mixed vertical structures and the cross-shelf gradient of the temperatures, indicating its effectiveness in simulating winter conditions. The higher temperatures near the open ocean are potentially due to the influx of warmer waters from the Gulf Stream. Interestingly, noticeable vertical gradients of the temperatures are observed near the estuary, showing warmer deep water than surface water. In the area, the denser, warmer saline waters from the ocean intrude into the deeper water of the estuarine zones, sliding beneath the outflowing freshwater from riverine discharges. The model proficiently captures these complex dynamics, as reflected in the similarity of the modeled temperature structure to the observed patterns. In summation, although the model results show errors in capturing the precise values of the temperatures, it can replicate the critical vertical structures of the temperatures in the SF and WS seasons both, reinforcing its credibility and utility in understanding important dynamics from the NY/NJ harbor to the continental shelf.

3.1.5. Salinity

In Fig. 8, the evaluation of the model's accuracy in predicting salinity levels during different seasons is illustrated through the biases and RMSEs. Specifically, Fig. 8(a) and (b) detail these metrics for the SF season, while Fig. 8(c) and (d) present the corresponding values for the WS season. In terms of biases, Fig. 8(a) and (c) reveal a general trend towards negative biases upstream of the Hudson River for the SF and WS seasons both, implying fresher water conditions. The biases downstream of the river show positive or negative biases depending on the SF season (positive) and WS season (negative). The RMSEs, as shown in Fig. 8(b) and (d), are higher downstream than upstream of the Hudson River for the SF and WS seasons. Overall, the model shows good skill in capturing the salinities along the Hudson River and NY/NJ harbor.

The model assessments through Figs. 3 to 8 underscore the critical influence of river discharge and DEM on the accurate simulation of hydrodynamic properties within the NY/NJ harbor. In addition, the model demonstrates higher accuracies in the SF season compared to the WS season. This seasonal difference is caused by extreme weather

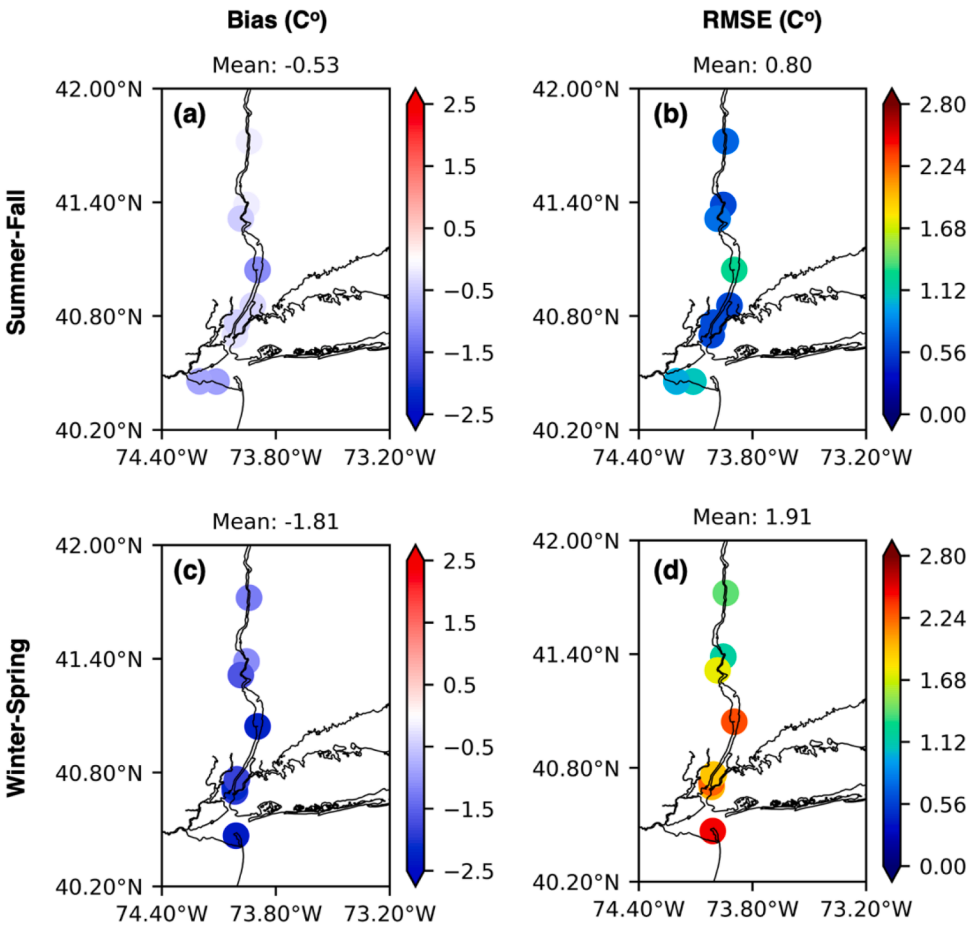

Fig. 6. The biases and RMSEs for the water temperatures from control runs (i.e., SF-CR and WS-CR). The top and bottom rows represent the statistical indexes for the summer-fall and winter-spring seasons, respectively.

conditions in the winter, which increase uncertainties from the forcing sources such as river discharge, precipitation, wind, and air pressure. The absence of an ice model and thermal source within the model, as discussed in Fig. 6, can exacerbate the degree of error during these colder months, further impeding model precision. Despite these challenges, our comparative analysis highlights the model's robust ability to simulate the essential processes and dynamics governing the important variables. The reliability of our model allows us to conduct a series of sensitivity experiments designed to investigate the impact of varying forcing sources on the model results.

3.2. Sensitivity experiments

The model evaluation in the previous section reveals that the model's predictive capabilities for the variables such as water levels, currents, temperature, and salinity are impacted by the uncertainties inherent in the forcing sources. With the availability of numerous large-scale models and a growing body of observational data for forcing sources in downscaling modeling, it is important to evaluate the sensitivity of model results to diverse forcing sources. Therefore, we investigate the dependencies and sensitivities of the different hydrodynamic variables to the different forcing sources in terms of the tide, surface forcing, open ocean boundary condition and river discharge in the following section.

3.2.1. Tide sources: FES2014, TPXO9 v1, and TPXO9 v5

To assess the sensitivities of the model results to different tidal forcing sources, bar plots are utilized to visualize the statistical parameters for different hydrodynamic variables across the experiments with different tidal models. Three different tidal models are considered for the sensitivity analysis, such as FES2014, TPXO9 v1, and TPXO9 v5, as summarized in Table 1.

Fig. 9 presents bar plots illustrating the mean Root Mean Square Errors (RMSEs) for total water levels and currents under various tidal forcing sources. In terms of total water levels in Fig. 9(a), the mean RMSEs from experiments using FES2014 (i.e., SF-CR and WS-CR) and TPXO9v5 (i.e., SF-TP5 and WS-TP5) are comparable. Specifically, the mean RMSEs are 9.27 cm for SF-CR and 9.65 cm for SF-TP5, while WS-CR and WS-TP5 show mean RMSEs of 14.39 cm and 14.68 cm, respectively. This comparison indicates that both tidal forcing sources result in a similar performance in predicting total water levels. During the SF season, the model result using TPXO9 v1 (e.g., SF-TP1) exhibits the highest mean RMSE (10.84 cm), which is approximately 1.57 cm higher than the SF-CR experiment. In the winter, the difference in the mean RMSEs between WS-CR (14.39 cm) and WS-TP1 (14.77 cm) is less pronounced, showing less than 1 cm. Supplementary Fig. 4, which compares M2 tidal constituents among the experiments, reveals a similar trend. The RMSEs for the M2 amplitude range from 1.83 cm (SF-CR) to 4.99 cm (SF-TP1) in the SF season, and from 2.25 cm (WS-CR) to 2.9 cm (WS-TP1) in the WS season. These findings indicate that the control runs consistently demonstrate the lowest RMSEs for both total water levels and the M2 tidal component across the experiments.

Regarding currents in Fig. 9(b), the model results using FES2014 and TPXO9v5 show comparable mean RMSEs, ranging from 12.50 cm/s (SF-CR) to 12.12 cm/s (SF-TP5) in the SF season, and from 13.66 cm/s (WS-CR) to 13.55 cm/s (WS-TP5) in the WS season. This similarity underscores the robustness of these tidal forcing sources in modeling current velocities. The experiments with TPXO9 v1 (i.e., SF-TP1 and WS-TP5) reveal that this experiment results in the highest mean RMSEs

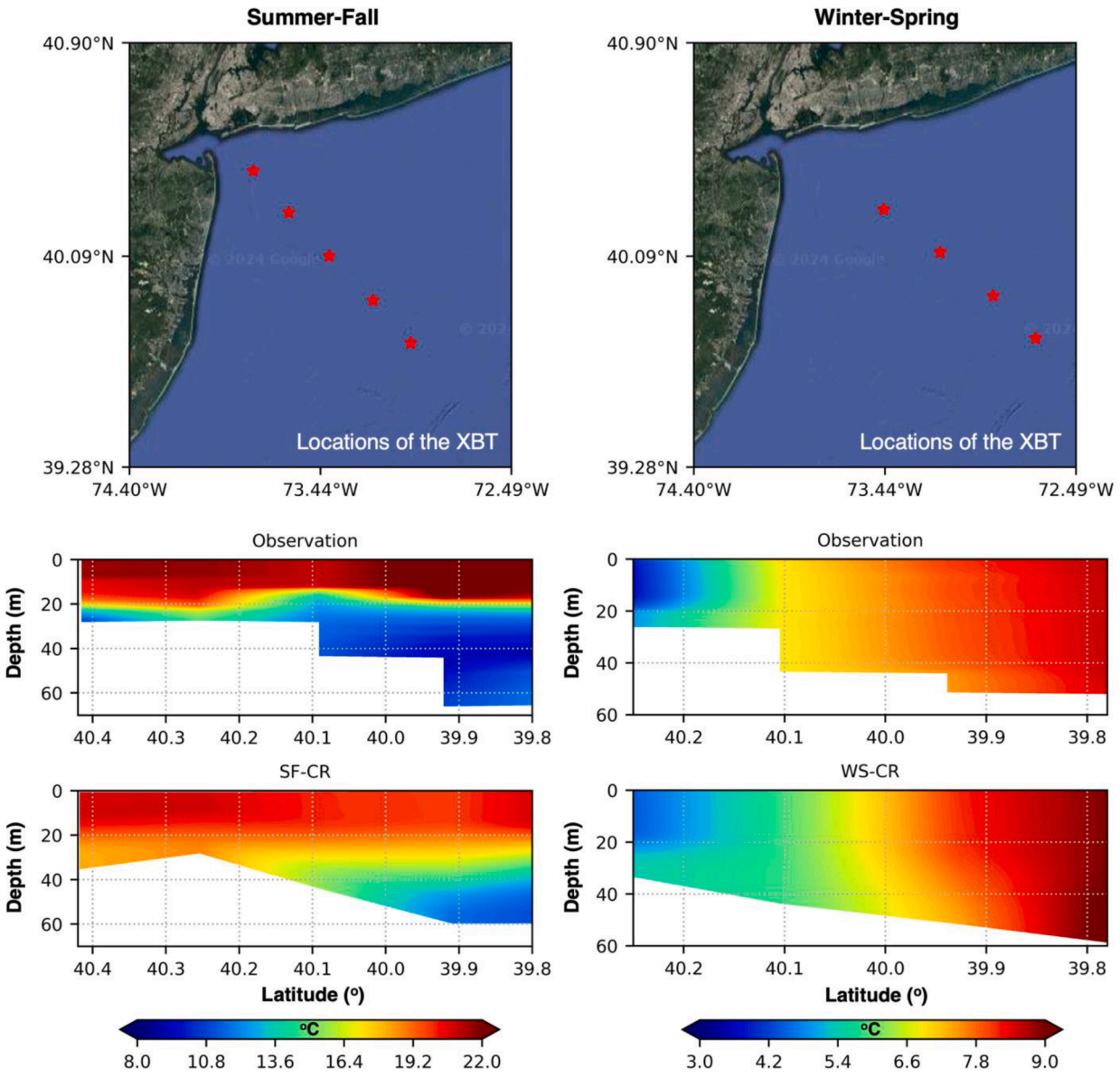

Fig. 7. The vertical profile of temperature from XBT and models for the summer (left column) and winter (right column).

compared to others, 1.43 cm/s higher in the summer and 0.65 cm/s higher than in the winter than control runs (i.e., SF-CR and WS-CR). The comparative analysis highlights the noticeable impact of the different tidal forcing sources on the total water levels and current in the inland region of the NY/NJ harbor.

In comparison to the currents observed in the inland channel (C2 in Fig. 2), the influence of varying tidal forcing sources on the shelf-scale currents is minimal. Fig. 10 presents two-dimensional maps of the RMSEs of surface currents, derived from comparisons with HF radar data. During the SF season, the spatial distribution of RMSEs remains consistent across different experimental setups, with higher values observed near the open boundary and the northeastern region. The mean RMSEs for the experiments during the SF season range from 15.34 cm/s (SF-CR) to 15.52 cm/s (SF-TP1). In the WS season, the mean RMSEs vary from 12.81 cm/s (WS-CR) to 12.96 cm/s (WS-TP1). The maximum discrepancies in error values are approximately 0.18 cm/s for the SF season and 0.15 cm/s for the WS season. These results highlight the relatively minor role that different tidal forcing sources play in affecting shelf-scale currents. The consistency in RMSE patterns across various tidal forcing scenarios indicates that other factors may have a more significant influence on the spatial variability and magnitude of surface currents in the studied area, which will be further discussed in Sections 3.2.2 and 3.2.3.

Fig. 11 illustrates the box plots of mean RMSEs for salinity and temperature under various tidal forcing sources. The figure provides a comparative analysis of how different tidal models influence the accuracy of temperature and salinity predictions. Fig. 11(a) reveals that the bar graphs for salinity predictions are of similar size across different experiments, suggesting that salinity predictions along the Hudson River are relatively insensitive to the choice of tidal models. The mean RMSEs for the salinity range from 1.59 PSU (SF-CR) to 1.64 PSU (SF-TP1) for the SF season and from 2.06 PSU (WS-CR) to 2.08 PSU (WS-TP5) for the WS season. In contrast, water temperature predictions in the NY/NJ harbor exhibit a clear dependency on the different tidal forcing sources, as shown in Fig. 11(b). This variation underscores the significant role that tidal models play in accurately simulating water temperature distributions in estuarine environments. Overall, the experiment utilizing FES2014 yields the lowest mean RMSEs for water temperature, with values of 0.8 °C in the SF season (SF-CR) and 1.91 °C in the WS season (WS-CR). The experiments using TPXO9v5 show the highest mean

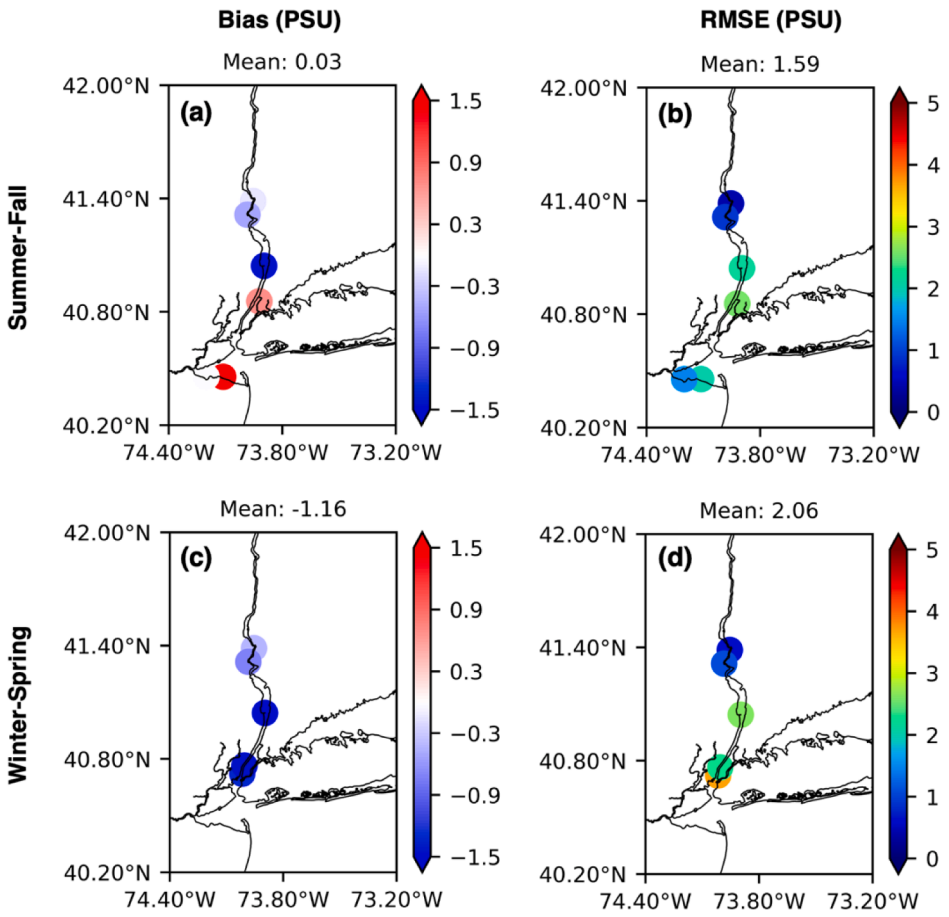

Fig. 8. The biases and RMSEs for the salinities from control runs (i.e., SF-CR and WS-CR). The top and bottom rows represent the statistical indexes for the summer-fall and winter-spring seasons, respectively.

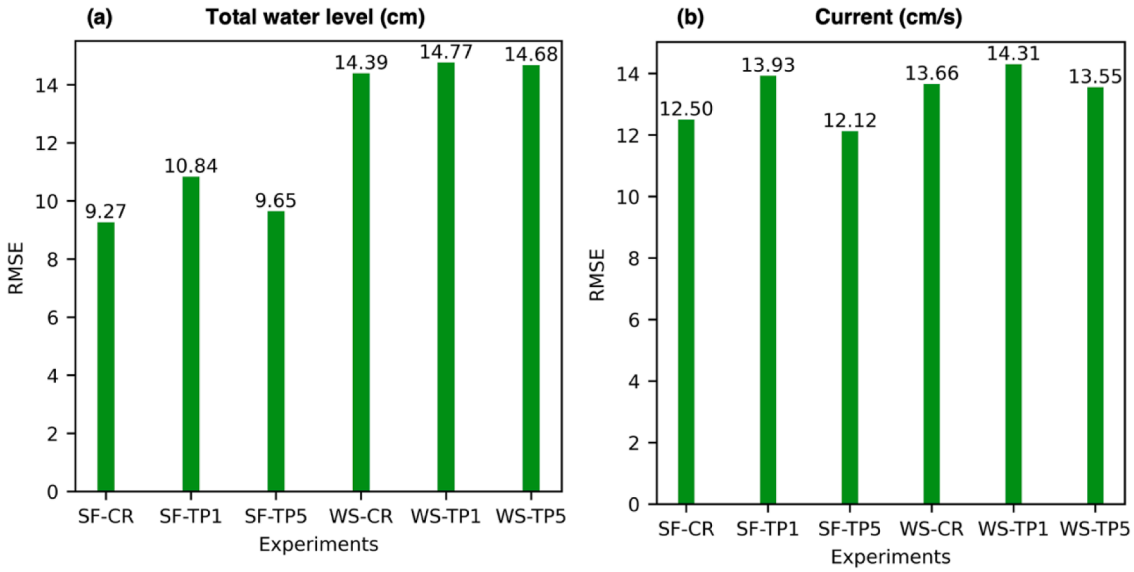

Fig. 9. The bar graph for the mean RMSEs of (a) the total water levels and (b) ocean currents from the different tidal forcing. The mean RMSE of the total water levels is calculated from the different total water level stations while the mean RMSE of the currents is calculated from different depths at the ocean current station as shown in Fig. 2(b).

RMSEs, with 0.86 °C for the SF season (SF-TP5) and 2.24 °C for the WS season (WS-TP5). The high differences in the errors are mainly observed upstream of the Hudson River, as shown in Supplementary Figure 5. In upstream river areas, the interaction between tidal flows and river discharge is more pronounced. Given that different tidal models present different tidal characteristics, the modeled temperature upstream of the river demonstrates a noticeable dependency on the chosen tidal model. For instance, the higher spatial resolution of FES2014 (1/16°) compared

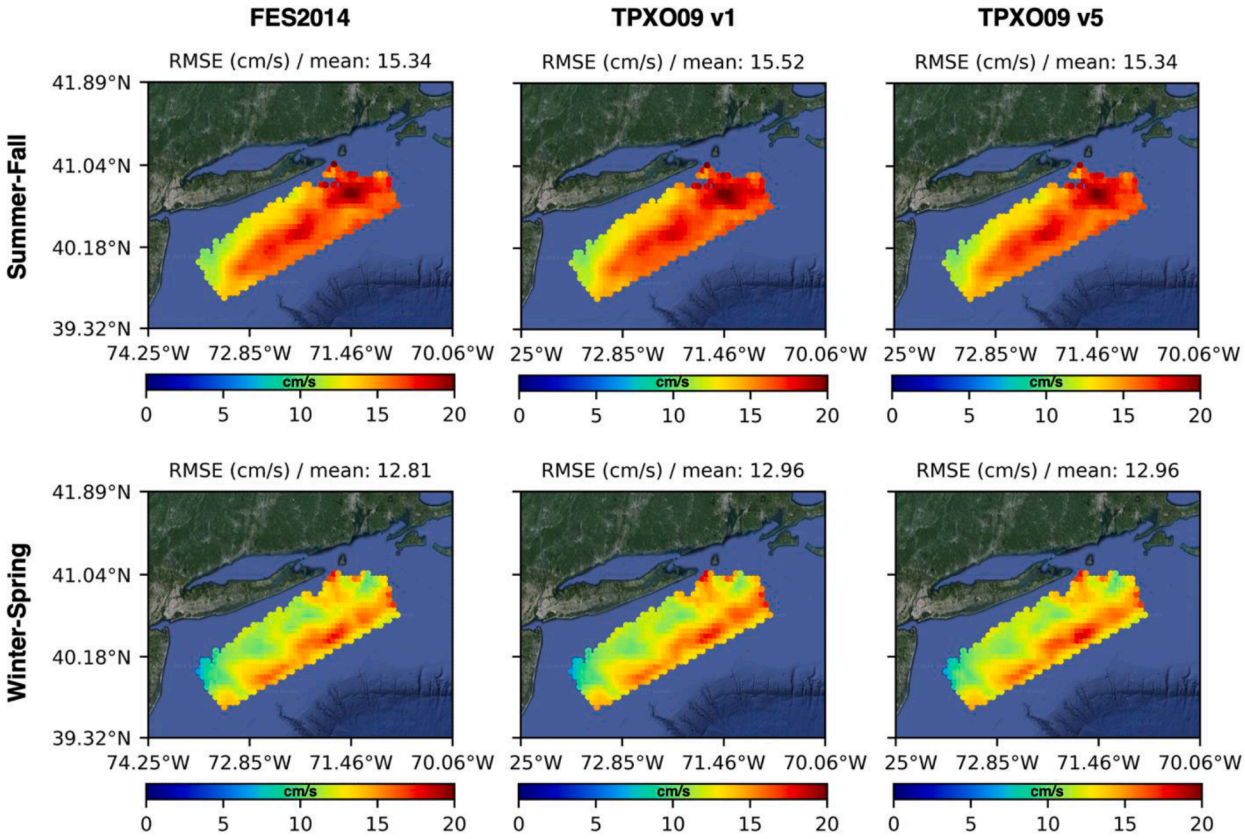

Fig. 10. Spatial map of RMSEs for the ocean surface currents from the different tidal forcing such as FES2014 (first column), TPXO9 v1 (second column) and TPXO9 v5 (third column). The top and bottom rows represent the spatial maps for the SF and WS seasons, respectively.

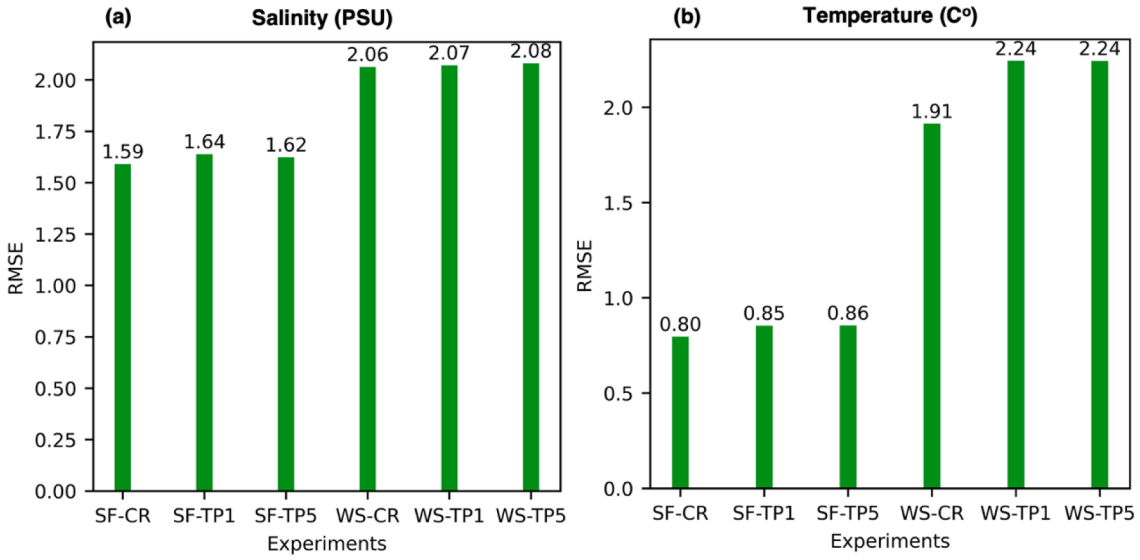

Fig. 11. The bar graph for the mean RMSEs of (a) the salinities and (b) water temperatures from the different tidal forcing. The mean RMSEs of the salinities and temperatures are calculated from the different temperature and salinity stations as shown in Fig. 2(c) and (d).

to TPXO9 v1 and v5 (1/6°) enables a more accurate representation of tidal dynamics in small-scale areas like the upstream Hudson River. This improved resolution enhances the accuracy of advection and redistribution of ocean temperature, emphasizing the dominant role of tide-driven processes in this region, where tidal energy strongly interacts with freshwater inflow. In addition, differences in representations of currents across the experiments can influence air-sea fluxes, further contributing to variability in temperature predictions within the upstream region. The impacts of the different tidal forcing sources are minor around the estuary and downstream of the Hudson River, showing similar errors in the area (Supplementary Fig. 5). This is because shelf-scale ocean currents exhibit minimal sensitivity to the choice of tidal models, as demonstrated in Fig. 10. Supplementary Figure 6 further demonstrates the minimal impact of various tidal

forcing sources on the vertical structure of temperatures across the continental shelf, showing similar patterns and magnitudes of the water temperature fields among the experiments. Therefore, we conclude that larger-scale regions, such as the continental shelf and estuary, are less sensitive to the resolution differences among the tidal models (e.g., from 1/16° to 1/6° spatial resolution in this study) compared to the upstream Hudson River. This reduced sensitivity results in similar ocean temperature predictions across the different tidal model experiments.

The different responses of the model results to the tidal models are attributed to the uncertainties inherent in the tidal models. Fig. 12 illustrates the errors in the M2 amplitude among the various tidal models, highlighting these discrepancies. In terms of tidal model accuracy, TPXO9 v1 shows higher errors of the M2 amplitudes at three different locations than FES2014 and TPXO9 v5. The reduced accuracy of TPXO9 v1 accounts for the higher errors observed in the SF-TP1 and WS-TP1 experiments, as shown in Fig. 9 and Supplementary Fig. 4.

The comparative analyses of model performance among the different experiments in Figs. 9 to 11 reveal that different tidal forcing sources significantly impact hydrodynamic variables. While the choice of a tidal model for salinity simulations is less critical, as indicated by the comparable model errors across different experiments, the selection of tidal forcing sources is crucial for accurately determining currents, water levels, and water temperature. Due to varying tidal forcing sources, the mean RMSEs change by up to 16.94 % for total water level, 14.93 % for current, 3.1 % for salinity, and 17.28 % for temperature in the NY/NJ harbor and on the Hudson River. This sensitivity experiment underscores the importance of carefully selecting tidal forcings to maximize fidelity to observed data, thereby enhancing the overall accuracy of coastal ocean models. Note that tidal effects can be modulated by interactions with river discharge, atmospheric forcing, and open ocean boundary conditions. For instance, tidal flows interacting with river discharge modulate mixing and advection processes, thereby influencing temperature and salinity distributions in the target area. Similarly, atmospheric factors such as wind stress and surface heat flux can amplify or suppress tidal dynamics, further impacting water levels and thermal structures. A comprehensive understanding of these interdependencies is critical for improving model accuracy and effectively interpreting the outcomes of sensitivity experiments.

3.2.2. *Surface forcing sources: HRRR, ERA5, and GFS*

The surface forcing of the coastal ocean model includes wind stress, air pressure, precipitation and heat flux, which are derived from large-scale atmospheric models. Fig. 13 presents bar plots depicting the mean RMSEs for total water levels and currents, evaluated under different atmospheric models. The atmospheric models considered include HRRR, ERA5, and GFS, as summarized in Table 1. This figure provides insights into how varying atmospheric input sources affect the model's performance in predicting water levels and currents. Fig. 13(a) displays the bar plot of mean RMSEs for total water levels. For the control run during the SF season (SF-CR), the lowest RMSE is 9.27 cm, compared to 9.36 cm for SF-ER and 9.69 cm for SF-GF. The maximum difference in the error during the SF season is approximately 0.42 cm between SF-CR and SF-GF. In the WS season, RMSEs are 14.39 cm for WS-CR, 13.60 cm for WS-ER, and 14.07 cm for WS-GF, with a maximum difference of about 0.79 cm between WS-CR and WS-ER. The higher sensitivity (e.g., the higher maximum difference in the RMSEs) of the water levels during the WS season to the atmospheric forcing can be caused by the different representations of the extreme weather among the different atmospheric forcing sources as the total water levels are more affected by the atmospheric forcing during the WS than the SF season. Nevertheless, the differences in RMSEs among the experiments are less than 1 cm for both seasons, indicating a minimal impact of different atmospheric models on total water level predictions. Fig. 13(b) illustrates the bar plot of mean RMSEs for currents. In the SF season, SF-GF shows the lowest RMSE of 12.06 cm/s, followed by 12.50 cm/s for SF-CR and 12.25 cm/s for SF-ER. The maximum difference in error is about 0.44 cm/s between SF-CR and SF-GF. During the WS season, RMSEs are 13.66 cm/s for WS-CR, 13.64 cm/s for WS-ER, and 13.89 cm/s for WS-GF, with a maximum difference of about 0.25 cm/s between WS-ER and WS-GF. Overall, the total water levels and currents in the inland region, as shown in Fig. 2, exhibit limited sensitivity to the different atmospheric models. The small differences in RMSEs across the experiments indicate that the choice of atmospheric model has a minor effect on the accuracy of total water levels and currents in these inland areas, although the spatiotemporal resolutions of the models are different.

The surface currents on the continental shelf exhibit a noticeable dependency on the different atmospheric models. This indicates that atmospheric forcing sources play an important role in shaping the accuracy of modeled surface currents in these regions. Fig. 14 presents two-dimensional maps of RMSEs for the surface currents in the continental shelf. In the SF season, the spatial patterns of RMSEs are similar

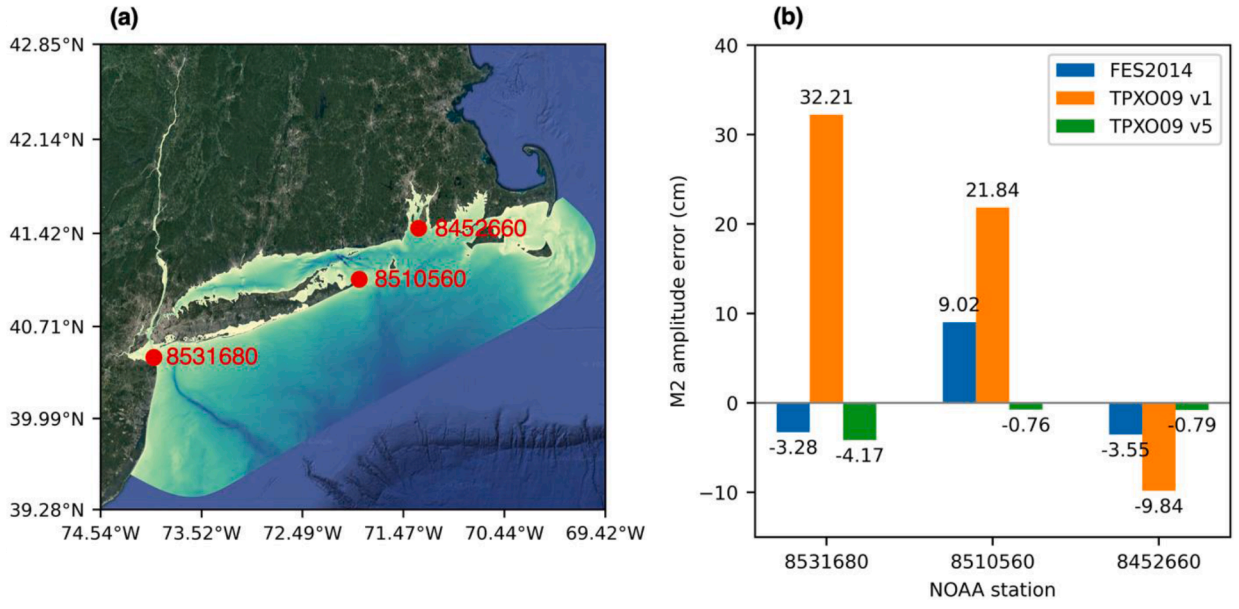

Fig. 12. (a) The locations of the NOAA stations used for the comparison of M2 amplitude. (b) The errors of M2 amplitude for the different tidal models.

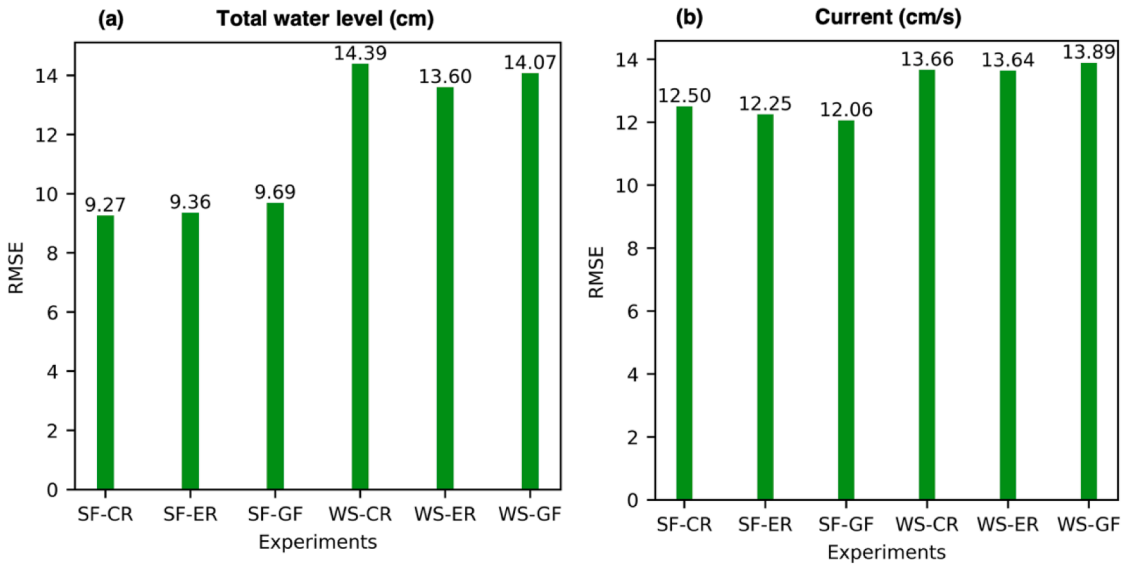

Fig. 13. The bar graph for the mean RMSEs of (a) the total water levels and (b) ocean currents from the different atmospheric forcing. The mean RMSE of the total water levels is calculated from the different total water level stations while the mean RMSE of the currents is calculated from different depths at the current station as shown in Fig. 2(b).

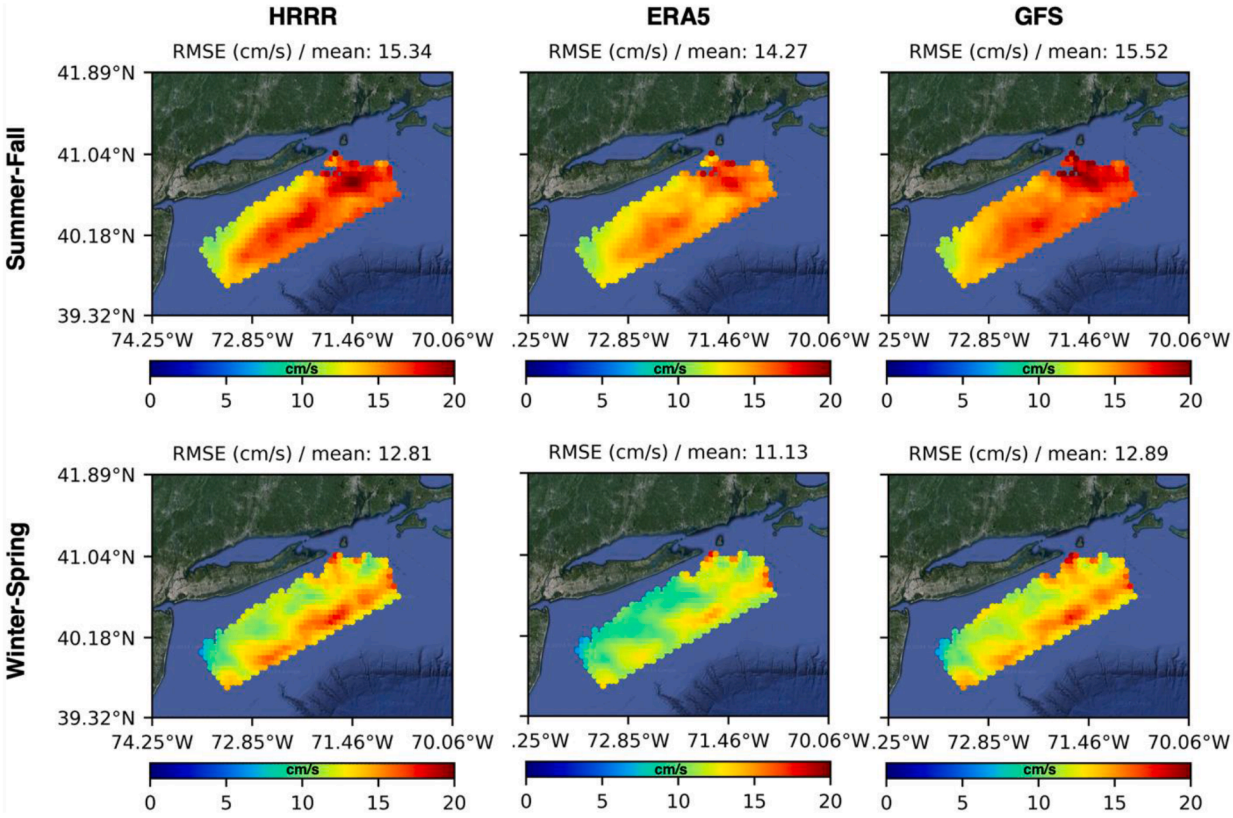

Fig. 14. Spatial map of RMSEs for the ocean surface currents from the different tidal forcing such as HRRR (first column), ERA5 (second column) and GFS (third column). The top and bottom rows represent the spatial maps for the summer-fall and winter-spring seasons, respectively.

across the different experiments, with higher values observed around the open boundary and the northeastern part of the study area. A detailed examination reveals that the experiment using ERA5 data yields the smallest mean RMSE of 14.27 cm/s, compared to 15.34 cm/s for HRRR and 15.52 cm/s for GFS. The maximum difference in error during the SF season is approximately 1.25 cm/s between SF-ER and SF-GF. During the WS season, the ERA5 model again produces the smallest mean RMSE of 11.13 cm/s, in contrast to 12.81 cm/s for HRRR and 12.89 cm/s for GFS. The maximum difference in error during the WS season is about 1.76 cm/s between SF-ER and SF-GF. These results underscore the significant impact of different atmospheric model inputs on shelf-scale currents. The variation in RMSEs highlights the importance of selecting appropriate atmospheric models to enhance the fidelity of surface current predictions in the continental shelf. The better

performance of ERA5 in both SF and WS seasons than other atmospheric forcing sources further emphasizes its reliability as a preferred atmospheric forcing source for accurate modeling of shelf-scale currents.

Fig. 15 presents bar plots of mean RMSEs for salinities and water temperatures under different atmospheric models, providing insights into how these models influence the accuracy of salinity and temperature predictions. Fig. 15(a) illustrates the bar plot for salinity. During the SF season, the experiment using the GFS (SF-GF) exhibits the highest RMSE of 1.64 PSU, compared to 1.59 PSU for SF-CR and 1.62 PSU for SF-GF. The maximum difference in error is about 0.05 PSU between SF-GF and SF-CR. In the WS season, the experiment with the HRRR (WS-CR) shows the highest RMSE of 2.06 PSU, in contrast to 1.98 PSU for WS-ER and 1.95 PSU for WS-GF, with a maximum difference of 0.11 PSU between WS-GF and WS-CR. Fig. 15(b) shows the bar plot of the mean RMSEs for water temperature. In the SF season, model results using HRRR (SF-CR) demonstrate the lowest mean RMSE of 0.80 °C, compared to 1.07 °C for SF-ER and 1.34 °C for SF-GF. The maximum difference in error is approximately 0.54 °C between SF-CR and SF-GF. During the WS season, the experiment with the ERA5 (WS-ER) produces the lowest mean RMSE of 1.74 °C, compared to 1.91 °C for both HRRR and GFS models. The maximum difference in error during the WS season is about 0.17 °C between WS-ER and the other models. Overall, these results highlight the influence of different atmospheric models on salinity and water temperature predictions. The salinities and temperature predictions demonstrate varying levels of accuracy across different models, with HRRR and ERA5 generally performing better in the SF season and WS season, respectively.

We attribute the different model errors for temperature directly to the uncertainties inherent in the atmospheric models. Fig. 16 illustrates the air temperature bias of various atmospheric models along the Hudson River, compared with observations from NOAA stations. The mean air temperatures biases from the models show negative values, ranging from −0.18 °C (HRRR and GFS) to −0.19 °C (ERA5) during the SF season. Although the biases are similar among the different models, the high-resolution results of HRRR can better capture the spatiotemporal variation of air temperature along the Hudson River, leading to improved model performance for the SF season as shown in Fig. 15(b). In the WS season, the mean air temperature biases from the different atmospheric models also show negative values, ranging from −0.28 °C (ERA5) to −0.74 °C (HRRR). Despite the high-resolution data provided by HRRR, its higher error in air temperature biases contributes to greater errors in the modeled temperature by the SCHISM model. This illustrates that while higher resolution can enhance certain aspects of model accuracy, it does not necessarily correct for inherent biases in the input source. Overall, these findings underscore the importance of addressing uncertainties in atmospheric model inputs to improve water temperature predictions in hydrodynamic models. The consistent negative biases observed across different models suggest a need for further calibration and validation to enhance the reliability of water temperature forecasts in coastal and estuarine environments. To improve the reliability of water temperature predictions, key parameters influencing air-sea fluxes, such as coefficients for shortwave and longwave radiation and latent and sensible heat fluxes, can be calibrated. These adjustments directly influence the heat exchange processes at the air-water interface. Additionally, applying bias corrections or spatial and temporal adjustments to the input atmospheric fields can further refine the accuracy of the model. Such efforts underscore the importance of calibrating both the input data and physical parameterizations to mitigate uncertainties in surface forcing.

We further investigate the temperature field in the open ocean using vertical profiles to understand the influence of different atmospheric forcing sources on water temperature distribution over water depth. When the vertical structures of the water temperature are well mixed during the WS season, the impacts of different atmospheric forcing sources on the vertical temperature profiles become more pronounced compared to the SF season. Fig. 17 illustrates the vertical temperature profiles along the XBT transect from different experiments. During the SF season, the water temperature profiles are similar across all experiments with slightly warmer surface waters around the estuary in SF-CR, indicating consistent temperature stratification with comparable values. In the WS season, the temperature profiles vary between experiments, showing a noticeable dependency on the different atmospheric forcing sources. This variability is due to the strong influence of atmospheric forcing on the vertical temperature structure, primarily through wind-induced mixing and processes such as downwelling and upwelling.

The analysis from Figs. 13 to 17 indicates that model errors for total water level, current, temperature, and salinity are generally lower during the SF season than in the WS season, regardless of the atmospheric models used. This increase in errors during the winter is attributed to seasonality and extreme weather conditions, which introduce greater variability and higher errors in the different atmospheric models. In addition, the water temperature fields are most sensitive to the different atmospheric forcing sources. Due to the different atmospheric forcing sources, the mean RMSEs change by up to 5.81 % for

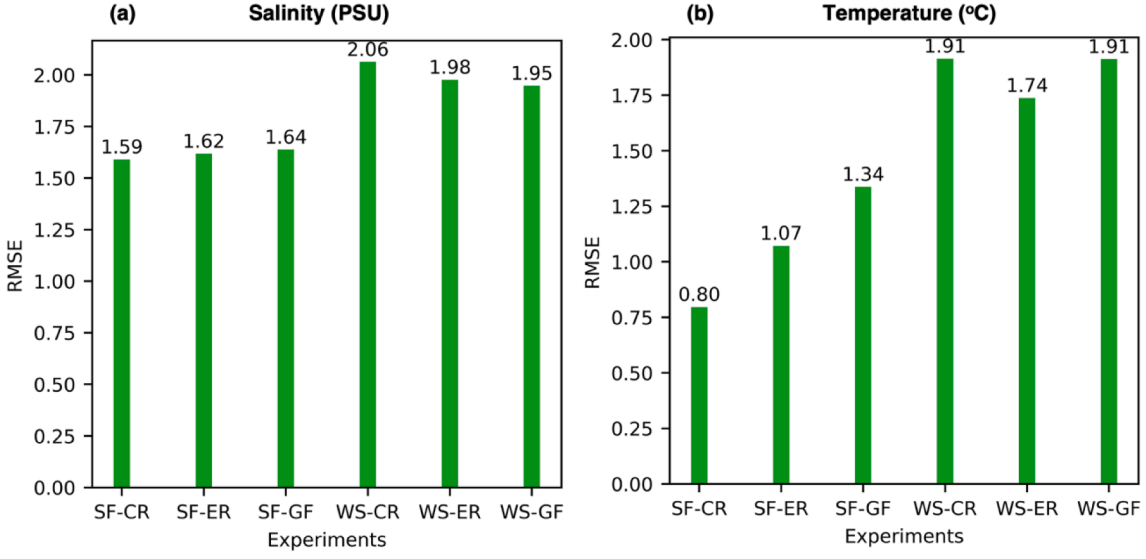

Fig. 15. The bar graph for the mean RMSEs of (a) the salinities and (b) water temperatures from the different atmospheric forcing. The mean RMSEs of the temperatures and salinities are calculated from the different temperature and salinity stations as shown in Fig. 2(c) and (d).

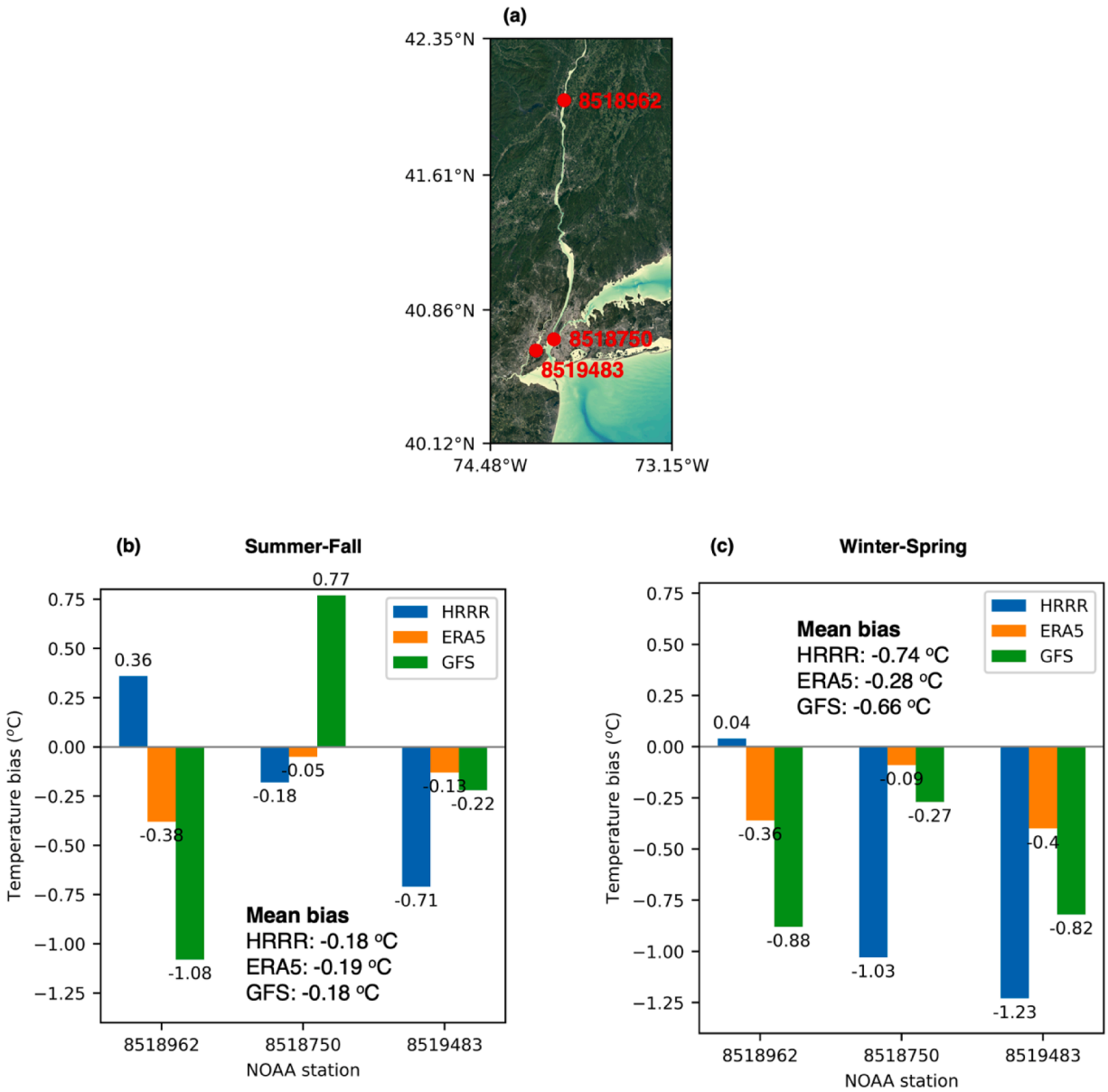

Fig. 16. (a) The locations of the NOAA stations used for the comparison of air temperature. (b) The biases of air temperatures for the summer-fall season. (c) The biases of air temperatures for the winter-spring season.

total water level, 3.65 % for current, 5.64 % for salinity, and 67.50 % for temperature in the NY/NJ harbor and on the Hudson River.

3.2.3. Open ocean boundary condition sources: CMEMS, HYCOM, and GRTOFS

The open ocean boundary conditions of coastal ocean models represent the sea surface height, ocean current, water temperature and salinity from larger scale ocean models. Fig. 18 presents bar plots of the mean RMSEs for total water levels and currents, analyzed under different oceanic forcing conditions. The sensitivity analysis includes three distinct oceanic models: CMEMS, HYCOM, and GRTOFS, as summarized in Table 1. Fig. 18(a) displays the bar plots of RMSEs for total water levels. The results indicate that the total water levels during the SF season are less impacted by the different oceanic forcing sources compared to the WS season. The mean RMSEs for the SF season range from 9.27 cm (SF-CR) to 9.38 cm (SF-GR and SF-HY). In contrast, the mean RMSEs for the WS season range from 14.39 cm (WS-CR) to 14.93 cm (WS-GR). The maximum difference in the error during the summer is approximately 0.11 cm while the maximum for the WS season is about 0.54 cm. The increased sensitivity of the water levels to different oceanic models arises from more extreme atmospheric conditions during the WS season. Increased wind stress and air pressure variations amplify variability in sea surface heights and currents, particularly at the open ocean boundary where the different ocean models (e.g., CMEMS, HYCOM, and GRTOFS) are used. Given the significant role of the open boundary conditions in propagating remote oceanic forcing to coastal sea levels (Park et al., 2022), these uncertainties lead to higher errors and sensitivities in the modeled water levels during the WS season compared to the SF season. Fig. 18(b) shows the mean RMSEs of currents across different depths at KVK (e.g., location of C2 in Fig. 2). The RMSEs range from 12.50 cm/s (SF-CR) to 12.73 cm/s (SF-GR) for the SF season, and from 13.66 cm/s (WS-CR) to 13.74 cm/s (WS-HY) for the WS season. The similarity in errors among the experiments suggests that the impacts of different ocean models on currents at KVK are minor. This indicates that the current predictions are relatively robust to the choice of oceanic models, with only slight variations observed across the different models.

Noticeable impacts of the different ocean models are observed on the currents in the continental shelf, as presented in Fig. 19. For both SF and

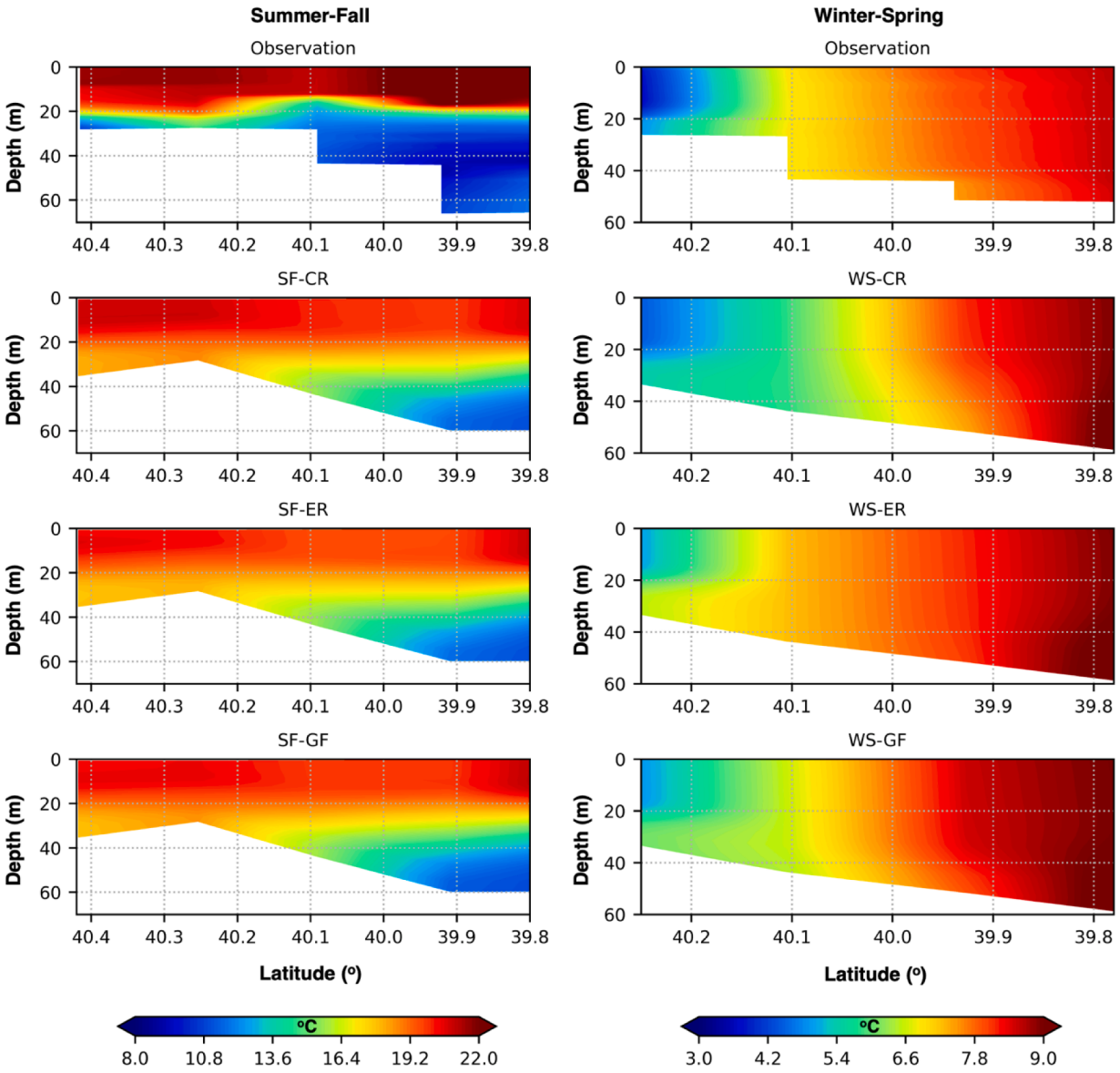

Fig. 17. The vertical profile of the temperatures from the XBT and experiments using different atmospheric forcing sources for the summer (left column) and winter (right column). The locations of the XBT points are presented in Fig. 7.

WS seasons, all experiments show high RMSEs around the open boundary and the northeast part of the model domain. However, the magnitude of these RMSEs varies among the different experiments. The experiments using CMEMS (i.e., SF-CR and WS-CR) demonstrate the lowest mean RMSEs, with values of 15.34 cm/s for the SF season and 12.81 cm/s for the WS season. This suggests that CMEMS provides more accurate surface current predictions in these regions. In contrast, the experiment utilizing HYCOM (i.e., SF-HY and WS-HY) results in the highest mean RMSEs, with values of 16.24 cm/s for the SF season and 14.18 cm/s for the WS season. The maximum differences in RMSEs between the experiments using CMEMS and HYCOM are approximately 0.9 cm/s for the SF season and 1.37 cm/s for the WS season. These differences underscore the optimal choice of ocean models for the better accuracy of modeled surface currents on the continental shelf.

Fig. 20 exhibits the mean RMSEs for salinity and temperature, analyzed under different ocean models. Through Fig. 20(a), it is observed that the RMSEs for salinity range from 1.59 PSU (SF-CR) to 1.66 PSU (SF-GR) during the SF season, and from 2.06 PSU (WS-CR and WS-GR) to 2.07 PSU (WS-HY) during the WS season. Overall, the experiments using CMEMS represent the lowest errors for both seasons. The sensitivity of salinity to different ocean models is attributed to the varying exchange of saline water through the open boundary, which influences salinity distribution in the model domain. The differences in the exchange of salt among large-scale oceanic models (e.g., HYCOM, GRTOFS and HYCOM) can be attributed to variations in model resolution, data assimilation methods, and input sources. For example, higher-resolution models or those with sophisticated data assimilation schemes are better at capturing mesoscale dynamics, such as eddies and boundary currents, which strongly influence salinity transport and mixing. Additionally, discrepancies in the quality and temporal frequency of observational data and atmospheric models used to constrain these models contribute to the variability of the salinity. Fig. 20(b) illustrates the mean RMSEs for temperature. The RMSEs for water temperature range from 0.80 °C (SF-CR) to 0.84 °C (SF-HY) during the summer, and from 1.88 °C (WS-GR) to 1.92 °C (WS-HY) during the WS season. The errors among the experiments are similar within each season, indicating a consistent performance across different oceanic models. However, there is a clear seasonal difference in the errors, with higher RMSEs observed during the WS season than in the SF season, regardless of the different ocean models. This suggests that water temperature

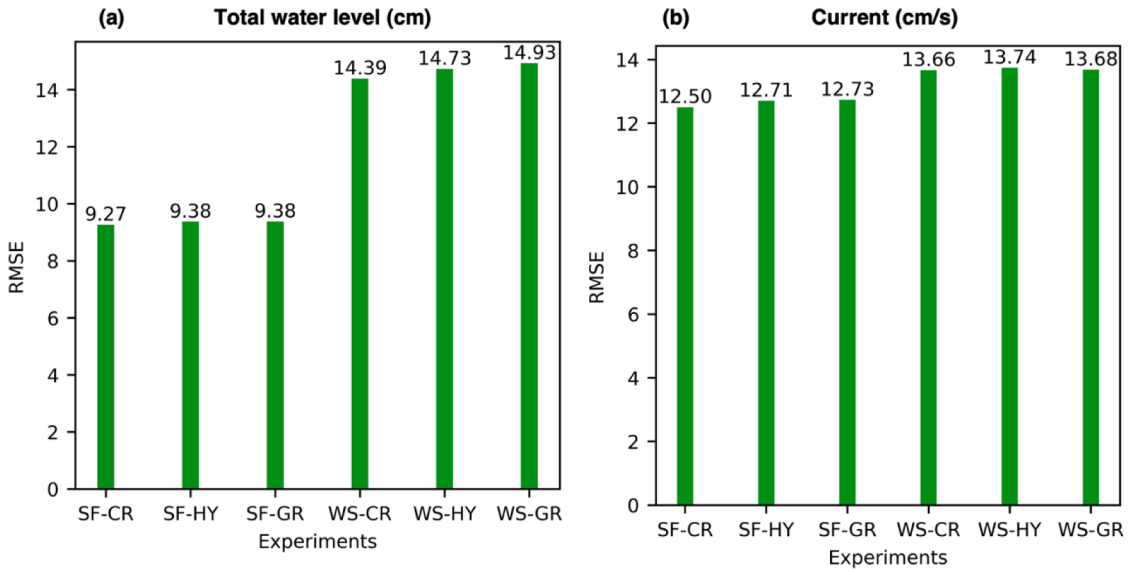

Fig. 18. The bar graph for the mean RMSEs of (a) the total water levels and (b) currents from the different ocean models. The mean RMSE of the total water levels is calculated from the different total water level stations while the mean RMSE of the currents is calculated from different depths at the current station as shown in Fig. 2(b).

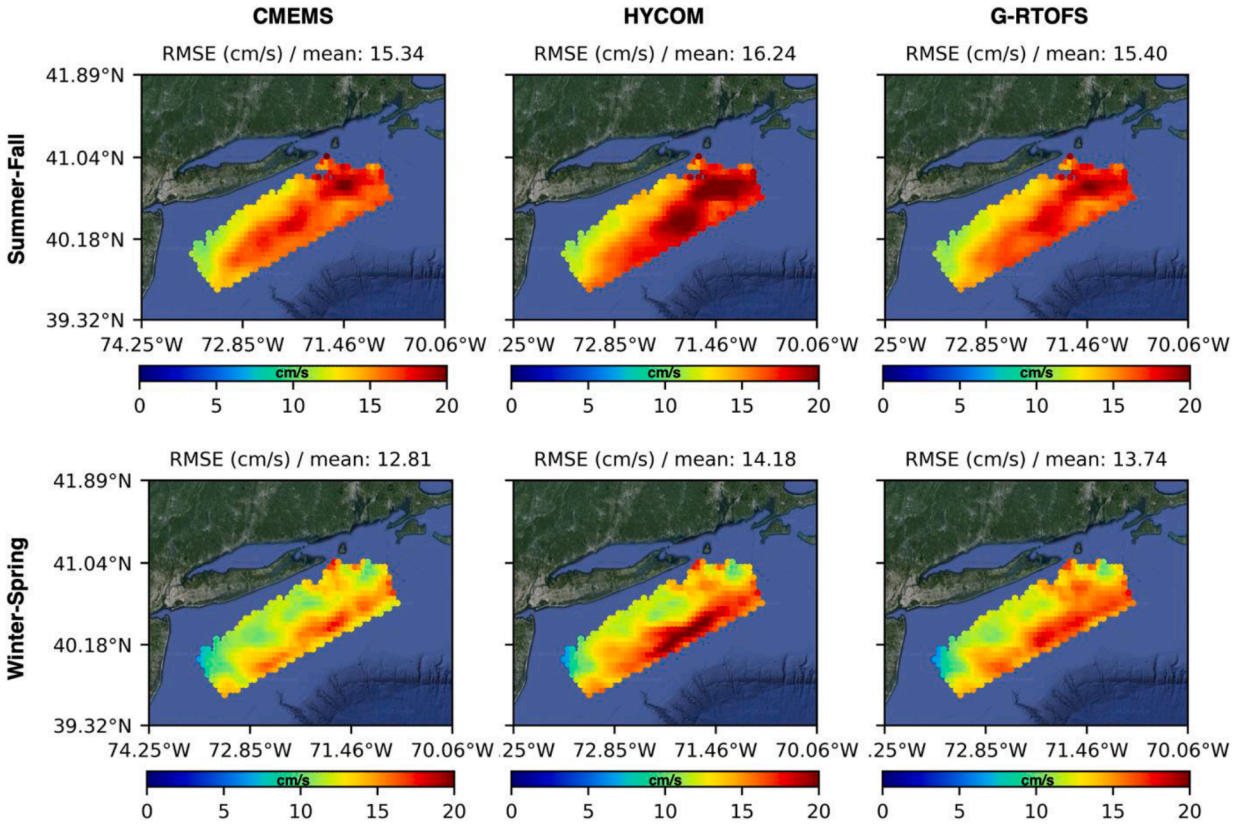

Fig. 19. Spatial map of RMSEs for the ocean surface currents from the different ocean models such as CMEMS (first column), HYCOM (second column) and G-RTOFS (third column). The top and bottom rows represent the spatial maps for the summer-fall and winter-spring seasons, respectively.

predictions are more challenging in the WS season due to increased seasonal variability and extreme conditions.

The vertical profile of temperatures along the XBT points in Fig. 21 clearly illustrates the varying impacts of different open boundary conditions from different ocean models on the temperature field in the open ocean. This analysis highlights how different oceanic models influence temperature stratification and distribution at different depths. During the SF season, when temperature stratification is pronounced, the experiments forced by HYCOM and GRTOFS (SF-HY and SF-GR) display warmer surface water (0 to 30 m) and colder deep water (40 to 70 m in offshore area) compared to the experiment forced by CMEMS (SF-CR). This indicates a stronger stratification in the SF season for the HYCOM and GRTOFS experiments, suggesting that these models simulate more distinct temperature layers inside the ocean. In the WS season, when the

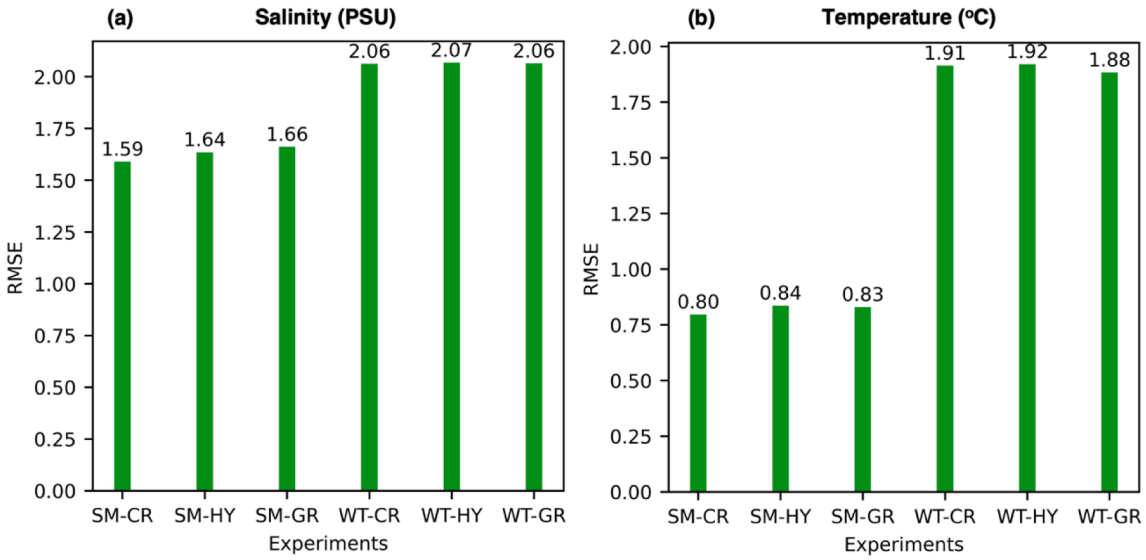

Fig. 20. The bar graph for the mean RMSEs of (a) the salinities and (b) water temperatures from the different ocean models. The mean RMSEs of the temperatures and salinities are calculated from the different temperature and salinity stations as shown in Fig. 2(c) and (d).

ocean temperature is well mixed over depth, noticeable differences in temperature distribution across the shelf are observed, particularly with warmer water intrusion discussed in Fig. 7. Generally, the WS-HY experiment shows warmer temperatures in the open ocean than other experiments, resulting in higher temperature intrusion beneath colder surface water around the estuary region. The vertical structure of temperatures from the different experiments demonstrates a clear dependency of shelf-scale temperature on the various oceanic forcing sources.

In summary, the model results (e.g., the total water levels, current, temperature and salinity) are less sensitive to the different oceanic forcing on the Hudson River and in the NY/NJ harbors while the influences of the different open boundary condition sources are pronounced on the continental shelf in terms of shelf-scale surface currents and cross-shelf gradients of temperature fields. Due to different open boundary conditions, the mean RMSEs change by up to 2.36 % for total water level, 1.84 % for current, 4.40 % for salinity, and 5.00 % for temperature on the Hudson River and in the NY/NJ harbor. However, during extreme weather events, water levels in inland channels become sensitive to different sources of the open boundary conditions. This sensitivity arises because open boundary conditions, such as sea surface height and currents, play a critical role in water level dynamics, acting as remote oceanic forcing (Park et al., 2022).

3.2.4. *River discharge sources: USGS and NWM*

Fig. 22 presents a bar plot and 2D map of the RMSEs for total water levels under two different river forcing sources: observed data from USGS and modeled data from NWM, as summarized in Table 1. Since the USGS data represent direct observations, this comparison allows us to assess how uncertainties in the NWM river discharge data influence the modeled hydrodynamic variables. Fig. 22(a) shows that the mean RMSEs for water levels across various stations are generally similar between the two forcing sources. For instance, the mean RMSEs during the SF season range from 9.27 cm (SF-CR) to 9.40 cm (SM-RF), while in the WS season, they range from 14.39 cm (WS-CR) to 14.54 cm (WS-RF). However, a closer inspection of individual stations reveals spatial variability in the impact of river discharge uncertainties, as illustrated in Fig. 22(b) Upstream stations, such as WL07 in the Hudson River, exhibit higher RMSEs under the NWM forcing compared to USGS data. In contrast, downstream stations and those around the estuary (e.g., WL01 to WL06) show minimal differences between the two data sources. These results suggest that uncertainties in river discharge data become increasingly significant in upstream regions, emphasizing the importance of accurate river discharge inputs for reliable water level predictions in these areas.

Fig. 23 presents the mean RMSEs for currents at different depths at KVK (location C2 in Fig. 2). The results indicate that the RMSEs range from 12.50 cm/s (SF-CR) to 12.92 cm/s (SM-RF) in the SF season and from 13.66 cm/s (WS-CR) to 13.74 cm/s (WS-RF) in the WS season. The difference in RMSEs between the two river discharge sources is more pronounced in the SF season (approximately 0.42 cm/s) compared to the WS season (0.18 cm/s). This seasonal discrepancy can be attributed to the higher errors in river discharges from the Hackensack and Passaic Rivers during summer, as shown in Fig. 24.

The stronger influence of these rivers on currents at KVK highlights the importance of accurate discharge estimates, particularly during the SF season when river discharge variability is more pronounced due to hurricanes. In comparison to inland currents, the influence of varying river discharge sources on shelf-scale currents is negligible, as presented in Supplementary Figure 7. During the SF season, the spatial distribution of RMSEs for shelf-scale currents remains largely consistent across the different experiments, with higher RMSE values observed near the open boundary and in the northeastern region of the domain. These results demonstrate that river forcing plays a minor role in influencing shelf-scale ocean currents, while its impacts are more significant in localized inland rivers and channels.

Fig. 25 presents a bar plot and 2D map of the RMSEs for salinity under different river discharge sources. In Fig. 25(a), the RMSEs for salinity range from 1.59 PSU (SF-CR) to 1.82 PSU (SF-RF) during the SF season and from 2.06 PSU (WS-CR) to 2.98 PSU (WS-RF) during the WS season. Notably, the differences in the RMSEs are larger in the WS season (0.92 PSU) than in the SF season (0.23 PSU), which can be attributed to higher uncertainties in the NWM data for the Hudson River during the season compared to the SF season, as shown in Fig. 24. This observation is particularly significant because most salinity measurements are concentrated along the Hudson River, where freshwater discharge strongly influences salinity distribution interacting with tidal salty water. In the upstream Hudson River, where tidal salty water barely reaches and salinity is near zero, the differences in RMSEs between experiments using USGS and NWM river discharges are negligible, as presented in Fig. 25(b). However, downstream, where tidal salty waters actively mix with freshwater, the RMSEs for salinity differ more prominently. This suggests that the uncertainties inherent in NWM river discharge outputs introduce greater errors downstream compared

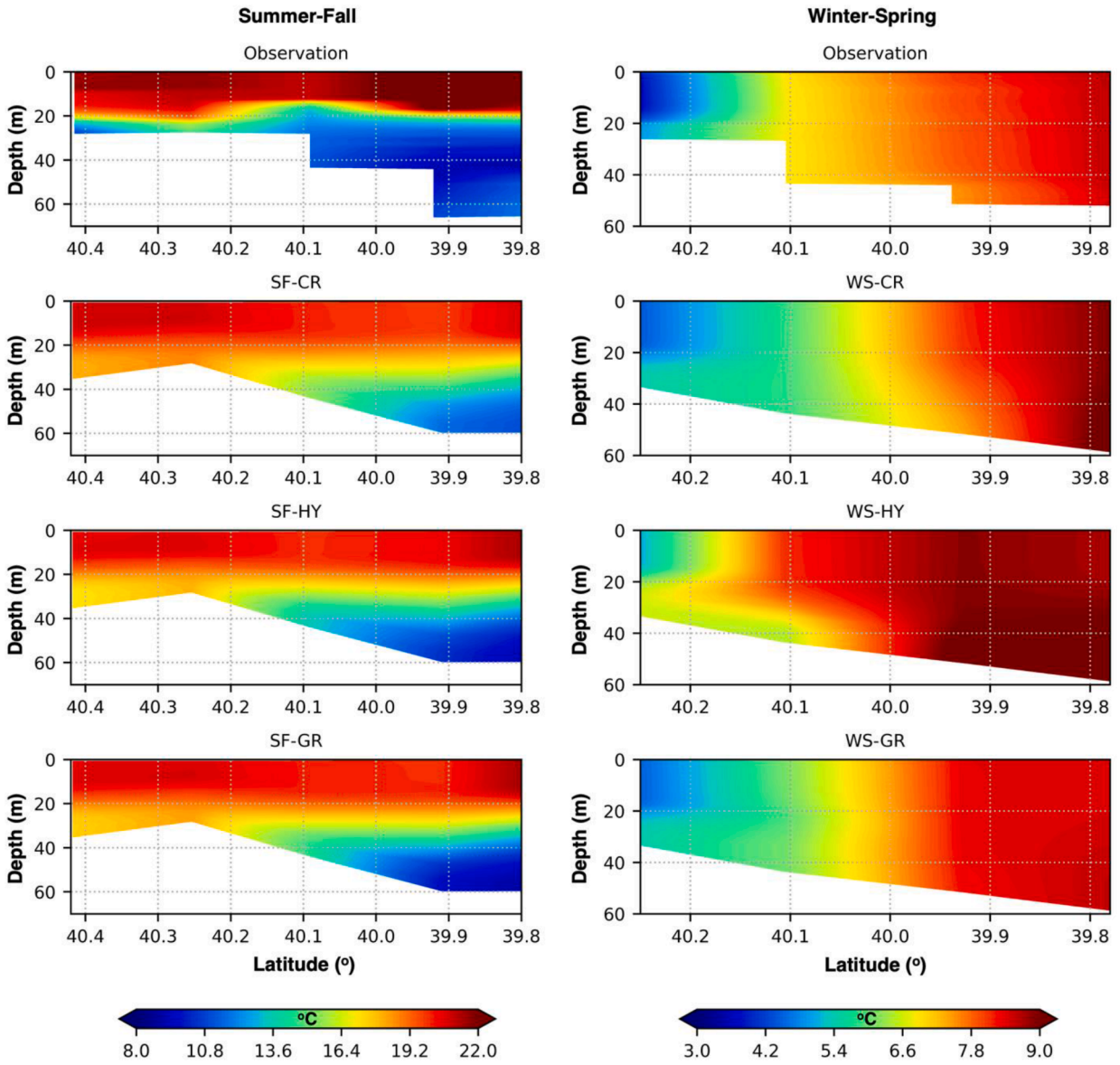

Fig. 21. The vertical profile of the temperatures from the XBT and experiments using different ocean models for the summer-fall season (left column) and winter-spring season (right column). The locations of the XBT points are presented in Fig. 7.

to USGS-based experiments that utilize observations.

Fig. 26 illustrates the mean RMSEs for water temperature, showing minimal differences across the experiments. The RMSEs range from 0.80 °C (SF-CR) to 0.83 °C (SF-RF) in the SF season and from 1.90 °C (WS-RF) to 1.91 °C (WS-CR) in the WS season. The similarity of errors within each season indicates consistent model performance across different river discharge sources. Furthermore, Supplementary Figure 8 demonstrates that the vertical temperature structure across the continental shelf remains largely unaffected by the choice of different river discharge sources, with similar patterns and magnitudes in all experiments.

The comparative analyses across Figs. 22 and 26 emphasize that the uncertainties in river discharge notably influence upstream total water levels, inland channel currents and downstream salinity, while water temperatures show negligible sensitivities to different river discharge sources. Quantitatively, the sensitivity experiment reveals that the mean RMSEs vary by up to 1.40 % for total water levels, 3.20 % for currents, 44.66 % for salinity, and 3.75 % for water temperature within the NY/NJ Harbor and the Hudson River. In contrast, the impacts of the uncertainties in the NWM data on shelf-scale ocean currents and the vertical profile of ocean temperature in the open ocean are minor or negligible. These findings underscore the critical role of river discharge uncertainties in hydrodynamic modeling, particularly the increased sensitivity of modeled salinity to variations in river discharge sources. Accurate representation of river discharge is therefore essential for improving model fidelity in regions where freshwater and tidal mixing dominate.

4. Discussion and conclusion

The findings from this study highlight the significant impacts of different forcing sources for tide, surfacing forcing, open ocean conditions and river discharges on the accuracy of coastal ocean models. By performing sensitivity experiments for total water levels, currents, salinity, and water temperature across various forcing scenarios, we investigate the distinct roles and contributions of these sources in coastal ocean conditions. First, we calibrate and evaluate the control runs (Section 3.1) to ensure the model used in this study accurately captures essential processes in the NY/NJ harbor. Comparing model results with an extensive set of observations, we establish high accuracy for the control runs, confirming the credibility of our findings.

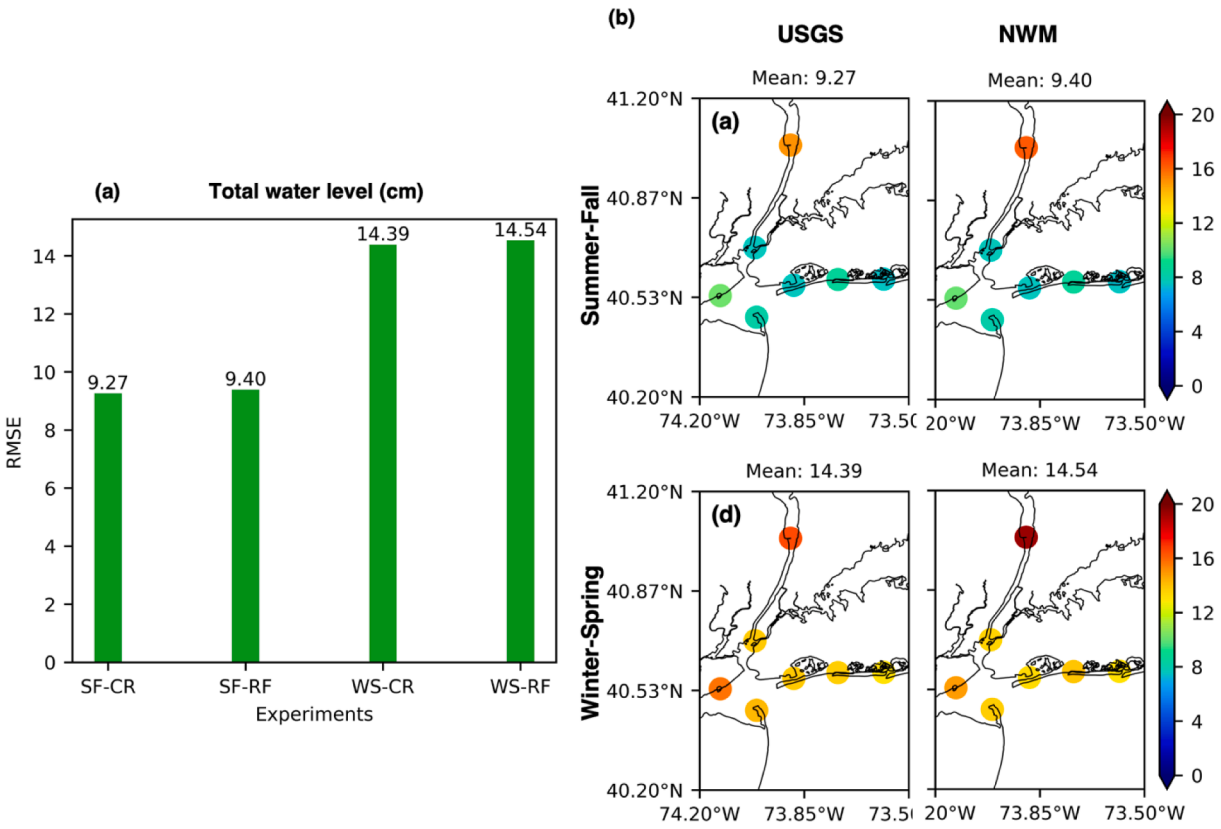

Fig. 22. The (a) bar graph and (b) 2D map for the mean RMSEs of the total water levels from different river discharge sources. The mean RMSE of the total water levels in (a) is calculated from the different total water level stations as shown in Fig. 2(b). The top and bottom rows in (b) represent the statistical parameters for the summer-fall and winter-spring seasons, respectively.

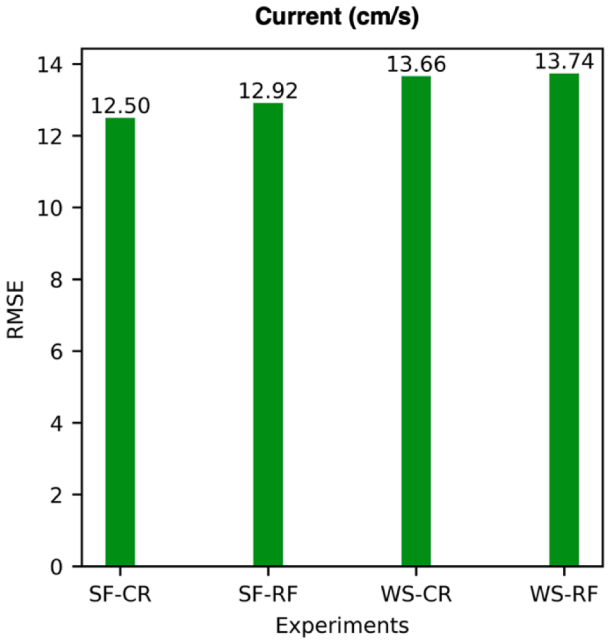

Fig. 23. The bar graph for the mean RMSEs of the ocean currents from the different ocean models. The mean RMSE of the currents is calculated from different depths at the current station as shown in Fig. 2(b).

Tide sources, such as FES2014, TPXO9 v1, and TPXO9 v5, significantly impact tidal components, total water levels, currents, and temperature in the inland areas (e.g., main rivers and estuaries of the NY/NJ harbor), with a minor effect on salinity. Due to varying tidal forcing sources, the mean RMSEs change by up to 16.94 % for total water level, 14.93 % for current, 3.1 % for salinity, and 17.28 % for water temperature in the NY/NJ harbor and on the Hudson River. Comparison with HF radar and XBT data suggests that surface currents and the vertical structure of temperature on the continental shelf are less affected by different tidal forcing sources, exhibiting similar RMSEs across the experiments with different tidal forcing sources.

Surface forcing sources, including HRRR, ERA5, and GFS, show varying degrees of influence on model predictions. While total water level, current and salinity predictions are less sensitive to the different atmospheric models, temperature predictions in the NY/NJ harbor demonstrate clear dependencies on different atmospheric forcing sources. Due to the different atmospheric forcing sources, the mean RMSEs change by up to 5.81 % for total water level, 3.65 % for current, 5.64 % for salinity, and 67.50 % for water temperature in the NY/NJ harbor and on the Hudson River. In addition, the surface currents on the continental shelf are notably sensitive to different atmospheric forcing sources. The vertical temperature structure is significantly impacted by wind-induced mixing during winter while the strong stratification of the ocean temperature for the summer is not sensitive to the different surface forcing sources.

Open ocean boundary condition sources, such as CMEMS, HYCOM, and GRTOFS, show minor impacts on the hydrodynamic variables in the NY/NJ harbor. Due to varying oceanic forcing sources, the mean RMSEs change by up to 2.36 % for total water level, 1.84 % for current, 4.40 % for salinity, and 5.00 % for water temperature in the NY/NJ harbor on the Hudson River. Oceanic forcing sources noticeably affect the ocean currents on the continental shelf, with mean RMSEs changing by up to 9.66 % depending on the different forcing sources. The different sources of the oceanic forcing also influence the intensity of the temperature

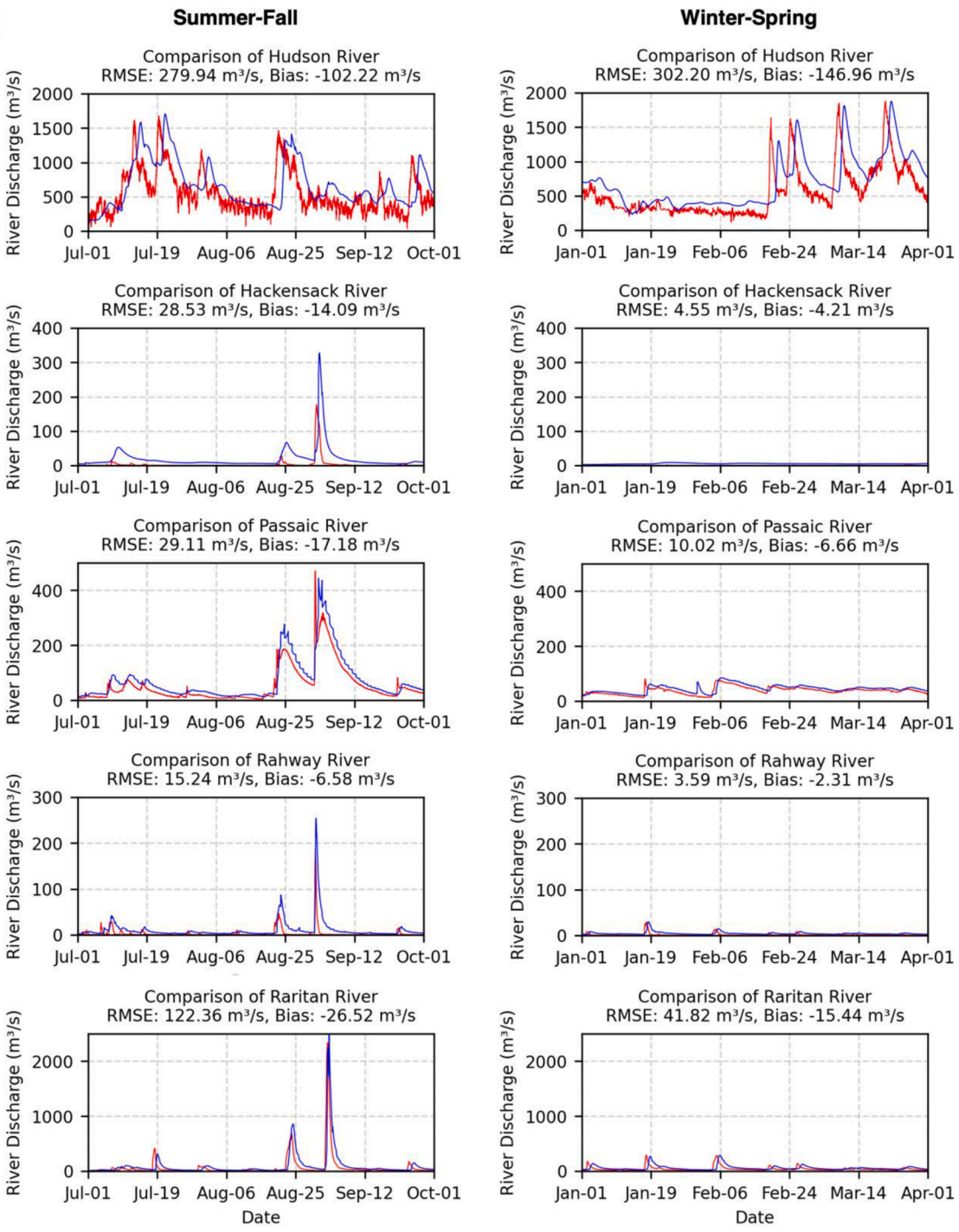

Fig. 24. Time histories of the rive discharges from Hudson, Hackensack, Passaic, Rahway and Raritan Rivers from USGS (red line) and NWM (blue line).

stratification offshore during the summer and the cross-shelf gradient of the temperature fields for the winter, where the ocean temperatures are well mixed over depth.

Different sources of river discharge data, such as USGS and NWM, affect upstream total water levels, inland channel currents, and downstream salinity, while the influence on water temperature is negligible in the NY/NJ harbor. Sensitivity experiments reveal that within the NY/NJ Harbor and the Hudson River, the mean RMSEs change up to 1.40 % for total water levels, 3.20 % for currents, 44.66 % for salinity, and 3.75 % for water temperature due to the different river discharge data sources. The different sources of the river discharge data have minimal or negligible effects on shelf-scale ocean currents and the vertical profiles of ocean temperature in open-ocean regions. Table 6 provides a summary of the maximum changes in RMSEs of hydrodynamic variables in the NY/NJ Harbor associated with different forcing sources.

Overall, our analysis demonstrates that different forcing sources play distinct roles in modulating coastal ocean model outputs. The sensitivity experiments conducted in this study are important for identifying optimal forcing sources that minimize errors and improve predictive capabilities, depending on target phenomena and dynamics. By understanding the specific contributions of tide, surface forcing, open ocean condition and river discharge, the accuracy and reliability of coastal ocean models can be further enhanced, supporting better-informed decision-making in coastal management and hazard mitigation.

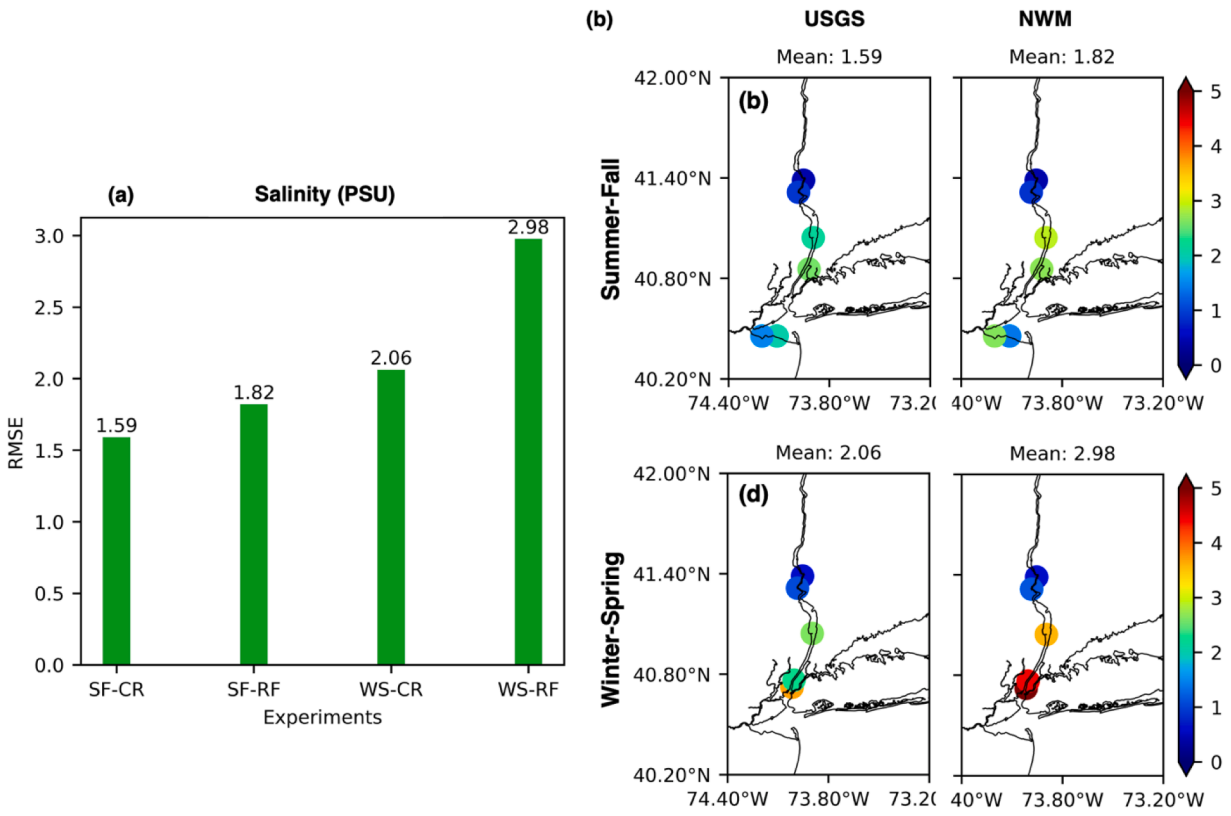

Fig. 25. The (a) bar graph and (b) 2D map for the mean RMSEs of the salinities from different river discharge sources. The mean RMSE of the salinities in (a) is calculated from the different total water level stations as shown in Fig. 2(b). The top and bottom rows in (b) represent the statistical parameters for the summer-fall and winter-spring seasons, respectively.

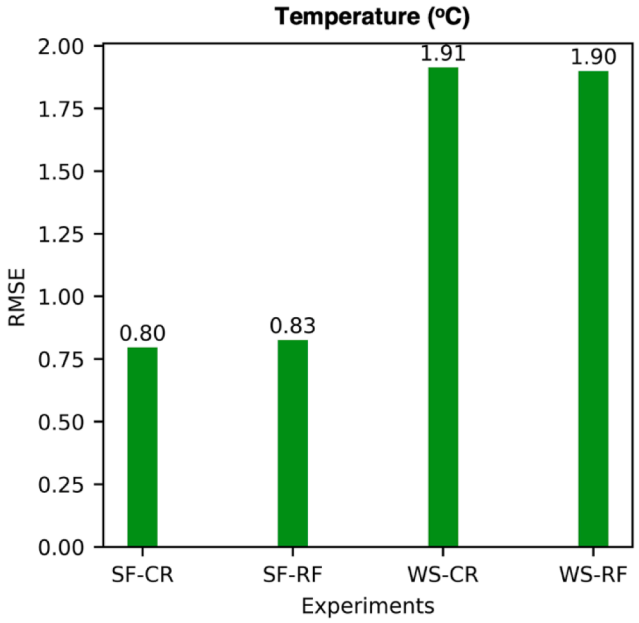

Fig. 26. The bar graph for the mean RMSEs of the water temperatures from the different ocean models. The mean RMSE of the water temperatures is calculated from the temperature stations as shown in Fig. 2(b).

Despite these findings, this study has limitations. Focusing on specific regions and time periods may limit the generalization of the results to other coastal environments and times of the year. Additionally, the models' performance in predicting long-term trends requires further investigation. Future studies should expand the geographic scope, incorporate diverse climatic conditions, and explore the long-term impacts of different forcing sources.

Table 6
Maximum change in RMSEs due to different forcing sources.

	Tide	Surface forcing	Open ocean boundary condition	River discharge
Total water level	16.94 %	5.81 %	2.36 %	1.40 %
Current	14.93 %	3.65 %	1.84 %	3.20 %
Salinity	3.10 %	5.64 %	4.40 %	44.66 %
Water temperature	17.28 %	67.50 %	5.00 %	3.75 %

In conclusion, with a growing body of large/global scale models and observations, coastal ocean modeling can benefit from using more forcing sources. Because different forcing sources uniquely affect hydrodynamic and thermodynamic properties, it is beneficial to choose the appropriate forcing source for better hindcast/forecast depending on simulation purposes. The model refinement and evaluation with the different forcing sources will reduce model uncertainty, boost confidence in the models, and enable better-informed decisions in managing safe and efficient marine navigation, forecasting coastal environments and mitigating coastal hazards under climate change.

CRediT authorship contribution statement

Kyungmin Park: Validation, Investigation, Data curation, Writing – review & editing, Writing – original draft, Visualization, Methodology, Formal analysis, Conceptualization. **Y. Joseph Zhang:** Writing – review & editing, Methodology. **Emanuele Di Lorenzo:** Writing – review &

editing, Funding acquisition. **Gregory Seroka:** Writing – review & editing. **Ayumi Fujisaki-Manome:** Writing – review & editing. **Shachak Pe'eri:** Writing – review & editing. **Saeed Moghimi:** Writing – review & editing. **John G.W. Kelley:** Writing – review & editing.

Declaration of competing interest

The authors declare that they have no known competing financial interests or personal relationships that could have appeared to influence the work reported in this paper.

Acknowledgments

This work was funded by the NOAA Unified Forecast System (UFS) MARACOOS grant UDR0000535 and NA22OAR4320150. We also acknowledge partial support from the 3CRS (www.3crs.org) NSF EPSCOR 2316271 and CEAR (www.cearhub.org) NOAA NA22NOS4690219 coastal resilience hubs. All model simulations were performed using the Texas Advanced Computing Center (TACC) Frontera at The University of Texas at Austin. This is the CIGLR contribution 1266.

Supplementary materials

Supplementary material associated with this article can be found, in the online version, at doi:10.1016/j.ocemod.2025.102598.

Data availability

Data will be made available on request.

References

Astudillo, O., Dewitte, B., Mallet, M., Rutllant, J.A., Goubanova, K., Frappart, F., Ramos, M., Bravo, L., 2019. Sensitivity of the near-shore oceanic circulation off Central Chile to coastal wind profiles characteristics. J. Geophys. Res.: Oceans 124 (7), 4644–4676.

Bastidas, L.A., Knighton, J., Kline, S.W., 2016. Parameter sensitivity and uncertainty analysis for a storm surge and wave model. Nat. Hazards Earth Syst. Sci. 16 (10), 2195–2210.

Bermúdez, M., Farfán, J.F., Willems, P., Cea, L., 2021. Assessing the effects of climate change on compound flooding in coastal river areas. Water Resour. Res. 57 (10) e2020WR029321.

Chassignet, E.P., Hurlburt, H.E., Smedstad, O.M., Halliwell, G.R., Hogan, P.J., Wallcraft, A.J., Baraille, R., Bleck, R., 2007. The HYCOM (hybrid coordinate ocean model) data assimilative system. J. Mar. Syst. 65 (1–4), 60–83.

Chen, X., 2012. A sensitivity analysis of low salinity habitats simulated by a hydrodynamic model in the Manatee River estuary in Florida, USA. Estuar. Coast. Shelf Sci. 104, 80–90.

Cosgrove, B., Gochis, D., Flowers, T., Dugger, A., Ogden, F., Graziano, T., Clark, E., Cabell, R., Casiday, N., Cui, Z., Eicher, K., 2024. NOAA's National Water Model: advancing operational hydrology through continental-scale modeling. JAWRA J. Am. Water Resour. Assoc. 60 (2), 247–272.

Dinápoli, M.G., Simionato, C.G., Moreira, D., 2020. Model sensitivity during extreme positive and negative surges in the Río de la Plata estuary: highlighting the need for an appropriate hindcast/forecast system. Weather Forecast. 35 (3), 1097–1112.

Dowell, D.C., Alexander, C.R., James, E.P., Weygandt, S.S., Benjamin, S.G., Manikin, G. S., Blake, B.T., Brown, J.M., Olson, J.B., Hu, M., Smirnova, T.G., Ladwig, T., Kenyon, J.S., Ahmadov, R., Turner, D.D., Duda, J.D., Alcott, T.I., 2022. The high-resolution rapid refresh (HRRR): an hourly updating convection-allowing forecast model. Part I: motivation and system description. Weather Forecast. 37 (8), 1371–1395. https://doi.org/10.1175/WAF-D-21-0151.1.

Egbert, G.D., Erofeeva, S.Y., 2002. Efficient inverse modeling of barotropic ocean tides. J. Atmos. Oceanic Technol. 19 (2), 183–204.

Ezer, T., Mellor, G.L., 2000. Sensitivity studies with the North Atlantic sigma coordinate Princeton ocean model. Dyn. Atmos. Oceans 32 (3–4), 185–208.

Fang, Y.C., Weingartner, T.J., Potter, R.A., Winsor, P.R., Statscewich, H., 2015. Quality assessment of HF radar–derived surface currents using optimal interpolation. J. Atmos. Ocean. Technol. 32 (2), 282–296.

Foreman, M.G.G., Henry, R.F., Walters, R.A., Ballantyne, V.A., 1993. A finite element model for tides and resonance along the north coast of British Columbia. J. Geophys. Res. Oceans 98 (C2), 2509–2531. https://doi.org/10.1029/92JC02470.

Garraffo, Z.D., Cummings, J.A., Paturi, S., Iredell, D., Spindler, T., Balasubramanian, B., Rivin, I., Kim, H.C., Mehra, A., 2020. RTOFS-DA: real time ocean-sea ice coupled three dimensional variational global data assimilative ocean forecast system. In: Astakhova, E. (Ed.), Research Activities in Earth System Modelling. World Climate Research Programme, Geneva.

Georgas, N., Yin, L., Jiang, Y., Wang, Y., Howell, P., Saba, V., Schulte, J., Orton, P., Wen, B., 2016. Multi-decadal, three-dimensional, hydrodynamic hindcast dataset for the Long Island Sound and New York/New Jersey Harbor estuaries. J. Mar, Sci, Eng 4, 48. https://doi.org/10.3390/jmse4030048.

Hersbach, H., Bell, B., Berrisford, P., Hirahara, S., Horányi, A., Muñoz-Sabater, J., Nicolas, J., Peubey, C., Radu, R., Schepers, D., Simmons, A., 2020. The ERA5 global reanalysis. Q. J. R. Meteorol. Soc. 146 (730), 1999–2049.

Huang, W., Zhang, Y.J., Wang, Z., Ye, F., Moghimi, S., Myers, E., Yu, H., 2022. Tidal simul. Revisit. Ocean Dyn. 72 (3), 187–205.

Hwang, P.A., 2018. High-wind drag coefficient and whitecap coverage derived from microwave radiometer observations in tropical cyclones. J. Phys. Oceanogr. 48 (10), 2221–2232.

Kernkamp, H.W., Van Dam, A., Stelling, G.S., de Goede, E.D., 2011. Efficient scheme for the shallow water equations on unstructured grids with application to the Continental Shelf. Ocean Dyn. 61, 1175–1188.

Klymak, J.M., Moum, J.N., Nash, J.D., Kunze, E., Girton, J.B., Carter, G.S., Lee, C.M., Sanford, T.B., Gregg, M.C., 2006. An estimate of tidal energy lost to turbulence at the Hawaiian ridge. J Phys. Ocean. 36 (6), 1148–1164.

Lane, R.R., Day Jr, J.W., Marx, B.D., Reyes, E., Hyfield, E., Day, J.N., 2007. The effects of riverine discharge on temperature, salinity, suspended sediment and chlorophyll a in a Mississippi delta estuary measured using a flow-through system. Estuar. Coast. Shelf Sci. 74 (1–2), 145–154.

Lellouche, J.M., Greiner, E., Galloudec, O.Le, Garric, G., Regnier, C., Drevillon, M., Benkiran, M., Testut, C.E., Bourdalle-Badie, R., Gasparin, F., Hernandez, O., 2018. Recent updates to the Copernicus Marine Service global ocean monitoring and forecasting real-time 1/12° high-resolution system. Ocean Sci. 14 (5)), 1093–1126.

Li, Y., Tang, C., Zhu, J., Pan, B., Anim, D.O., Ji, Y., Yu, Z., Acharya, K., 2015. Parametric uncertainty and sensitivity analysis of hydrodynamic processes for a large shallow freshwater lake. Hydrol. Sci. J. 60 (6), 1078–1095.

Li, G., Iskandarani, M., Hénaff, M.L., Winokur, J., Le Maître, O.P., Knio, O.M., 2016. Quantifying initial and wind forcing uncertainties in the Gulf of Mexico. Comput. Geosci. 20, 1133–1153.

Lyard, F.H., Allain, D.J., Cancet, M., Carrère, L., Picot, N., 2021. FES2014 global ocean tide atlas: design and performance. Ocean Sci. 17 (3), 615–649.

Merz, B., Blöschl, G., Vorogushyn, S., Dottori, F., Aerts, J.C., Bates, P., Bertola, M., Kemter, M., Kreibich, H., Lall, U., Macdonald, E., 2021. Causes, impacts and patterns of disastrous river floods. Nat. Rev. Earth Environ. 2 (9), 592–609.

Munk, W., Wunsch, C., 1998. Abyssal recipes II: energetics of tidal and wind mixing. Deep-Sea Res. 45, 1977–2010.

National Weather Service (NWS) New York, 2022a. Area Forecast Discussion. Jan 31, 2022, accessible at. https://mesonet.agron.iastate.edu/wx/afos/p.php?pil=AFDOKX&e=202201312111.

National Weather Service (NWS) New York, 2022b. Area Forecast Discussion. Feb 1, 2022, accessible at. https://mesonet.agron.iastate.edu/wx/afos/p.php?pil=AFDOKX&e=202202012209.

Park, K., Federico, I., Di Lorenzo, E., Ezer, T., Cobb, K.M., Pinardi, N., Coppini, G., 2022. The contribution of hurricane remote ocean forcing to storm surge along the southeastern US coast. Coast. Eng. 173, 104098.

Park, K., Di Lorenzo, E., Zhang, Y.J., Wang, H., Ezer, T., Ye, F., 2024. Delayed coastal inundations caused by ocean dynamics post-Hurricane Matthew. npj Clim. Atmos. Sci. 7 (1), 5.

Schroeter, S., Sandery, P.A., 2022. Large-ensemble analysis of Antarctic sea ice model sensitivity to parameter uncertainty. Ocean Model. 177, 102090.

Seroka, G., Kelley, J., Sienkiewicz, J., Seaton, C., Anderson, E.J., Allen, A., Forbes, C., Fujisaki-Manome, A., Haas, K.A., Lindley, C., Roman, D., Weston, A., 2022. Unified Forecast system (UFS) Coastal Applications Team - water quantity marine navigation sub-application Tiger Team: report. NOAA Tech. Memo. (34), 1–27. https://doi.org/10.25923/x7zr-nj33. NOS.

Seroka, G., Fujisaki-Manome, A., Kelley, J., Pe'eri, S., Sienkiewicz, J., Feyen, J., Doty, O., Ide, K., Gramp, B., Ogden, F., Fanara, T., Myers, E., Moghimi, S., Cockerill, T., Wu, W., Anderson, E., Huelse, K., Forbes, C., Liu, Y., John, S., Di Lorenzo, E., Park, K., Wipperfurth, S., Sannikova, N., Titov, V., Wei, Y., Akan, C., Mani, S., Lindley, C., 2024. UFS coastal applications team report round 1 summary of a unified forecast system model evaluation for marine navigation. NOAA Tech. Memo. NOS 36/NWS04/OAR04. https://doi.org/10.25923/nws6-kx30. May 2024.

Trotta, F., Federico, I., Pinardi, N., Coppini, G., Causio, S., Jansen, E., Iovino, D., Masina, S., 2021. A relocatable ocean modeling platform for downscaling to shelf-coastal areas to support disaster risk reduction. Front. Mar. Sci. 8, 642815.

Umlauf, L. and Burchard, H., 2003. A generic length-scale equation for geophysical turbulence models.

Warder, S.C., Horsburgh, K.J., Piggott, M.D., 2021. Adjoint-based sensitivity analysis for a numerical storm surge model. Ocean Model. 160, 101766.

Warner, J.C., Geyer, W.R., Ralston, D.K., Kalra, T., 2020. Using tracer variance decay to quantify variability of salinity mixing in the Hudson River estuary. J. Geophys. Res.: Oceans 125 (12) e2020JC016096.

Wei, E. and Chen, M., 2001. Hydrodynamic model development for the port of New York/New Jersey water level and current nowcast/forecast model system.

Xu, J., Zhang, A., Kurapov, A., Seroka, G. and Bayler, E., 2022. Implementation of the West Coast Operational Forecast System (WCOFS) and the semi-operational nowcast/forecast skill assessment.

Ye, F., Zhang, Y.J., Yu, H., Sun, W., Moghimi, S., Myers, E., Nunez, K., Zhang, R., Wang, H.V., Roland, A., Martins, K., 2020. Simulating storm surge and compound flooding events with a creek-to-ocean model: importance of baroclinic effects. Ocean Model. 145, 101526.

Yu, H.C., Zhang, Y.J., Jason, C.S., Terng, C., Sun, W., Ye, F., Wang, H.V., Wang, Z., Huang, H., 2017. Simulating multi-scale oceanic processes around Taiwan on unstructured grids. Ocean Model. 119, 72–93.
Zhang, Y.J., Ateljevich, E., Yu, H.C., Wu, C.H., Jason, C.S., 2015. A new vertical coordinate system for a 3D unstructured-grid model. Ocean Model. 85, 16–31.
Zhang, Y.J., Ye, F., Stanev, E.V., Grashorn, S., 2016. Seamless cross-scale modeling with SCHISM. Ocean Model. 102, 64–81.
Zhang, Y.J., Anderson, J., Park, K., Wu, C.H., Wipperfurth, S., Anderson, E., Pe'eri, S., Beletsky, D., Titze, D., Di Lorenzo, E., Moghimi, S., 2024. Debunking common myths in coastal circulation modeling. Ocean Model. 190, 102401.
Zhao, X., Shen, Z.Y., Xiong, M., Qi, J., 2011. Key uncertainty sources analysis of water quality model using the first order error method. Int. J. Environ. Sci. Technol. 8, 137–148.